

Shining Light on Microtubule Nucleation:
FRET Measurements
with Bayesian Analysis of FLIM

A DISSERTATION PRESENTED
BY
BRYAN THOMAS KAYE
TO
THE SCHOOL OF ENGINEERING AND APPLIED SCIENCES

IN PARTIAL FULFILLMENT OF THE REQUIREMENTS
FOR THE DEGREE OF
DOCTOR OF PHILOSOPHY
IN THE SUBJECT OF
APPLIED PHYSICS

HARVARD UNIVERSITY
CAMBRIDGE, MASSACHUSETTS
MAY 2017

© 2017 - BRYAN KAYE
ALL RIGHTS RESERVED.

Shining Light on Microtubule Nucleation: FRET Measurements with Bayesian Analysis of FLIM

ABSTRACT

The mitotic spindle is a self-organizing structure that segregates chromosomes during cell division. The spindle is composed of microtubules and accessory proteins, and microtubules are composed of the protein tubulin. Understanding microtubule nucleation is critical to understanding the assembly and maintenance of the mitotic spindle. Microtubules are nucleated by accessory proteins called microtubule nucleators, which have been proposed to be activated by microtubules. To test this hypothesis, we measure the activity of nucleators not bound to microtubules by studying the gradient in polymer concentrations leaving the spindle boundary. We combine FRET and microscopy to measure the concentration of polymer in Xenopus egg extracts. To detect FRET, we measure the lifetime of the excited state of the donor fluorophore, a technique commonly referred to as FLIM. We developed a Bayesian framework for analyzing FLIM measurements.

LIST OF FIGURES

Figure 2.1. Photon arrival-time histograms are composed of the sum of two exponential distributions. (A) Photon arrival histogram composed of two exponential distributions, with a short-lifetime fraction f_s , a long-lifetime fraction f_l , and a background fraction $f_B = (1 - f_s - f_l)$ (B) Inferred posterior distribution generated from data in Fig 2.1A.

Figure 2.2. Low-Photon Regime. (A) Control dyes having known long (Coumarin 153) and short (Erythrosin B) lifetimes were mixed at a fixed ratio. From the measured master curve of photon arrival times, a variable number of photons are randomly sampled, generating histograms with a variable number of photons. (B) Bias in the estimated short-life photon fraction, f_s , decreases with increasing photon number. Data points represent the average of the posterior mean (squares) or mode (circles) for 300 independent samplings for each photon count. Error bars are s.e.m. (C) Black circles: measured sample standard deviations from data in Fig 2B averaged across the 300 independent samplings. The sample standard deviation decreases approximately as n_{photon}^{-b} . Power law fit to $a \times x^b$ for all but the four lowest values of n_{photon} shown in gray, with $a = 0.04 \pm 0.01$ and $b = -0.48 \pm 0.04$ (95% confidence interval).

Figure 2.3. Low-fraction regime. (A) Samples of dyes with short-lifetime (Erythrosin B) and long-lifetime (Coumarin 153) were prepared, and fluorescence lifetime measurements were collected for each dye separately, leading to separate master photon histograms. Test histograms were constructed by randomly sampling a fixed number of photons, with varying fractions being drawn from the master lists of short-lifetime and long-lifetime photons. These histograms were then analyzed in order to estimate the fraction of short-lifetime photons, f_s . (B) The estimated short-lifetime fraction, f_s , varies linearly with the constructed short-lifetime fraction for three different total photon numbers, with a small offset. Squares: estimate from posterior mode. Dots: estimate from posterior mean. Dashed lines: linear fits with slopes 0.9933 ± 0.0026 , 1.0085 ± 0.0024 , and 1.0106 ± 0.0031 , and offsets of $0.002000 \pm 0.0484 \times 10^{-4}$, $0.004400 \pm 0.0814 \times 10^{-4}$, and $0.009500 \pm 0.1992 \times 10^{-4}$ for low, medium, and high intensities respectively (95% confidence interval). Intensities correspond to data collected at 1.5×10^5 , 1.2×10^6 , and 4.8×10^6 counts per second, for low, medium, and high intensity respectively. Inset: Data from main figure shown on a log-log scale. (C) Changes in the estimated short-lifetime fraction track the known changes in the short-lifetime fraction. Squares: estimate from posterior mode. Dots: estimate from posterior mean. Dashed lines: Linear fits with slopes of 0.9573 ± 0.1895 , 1.0013 ± 0.1445 , and 0.9580 ± 0.1717 , and offsets of $(0.2332 \pm 0.3712) \times 10^{-5}$, $(0.3215 \pm 0.3088) \times 10^{-5}$, and $(0.4617 \pm 0.4286) \times 10^{-5}$ for low, medium, and high intensities respectively (95% confidence interval).

Figure 2.4. *In vivo* Testing. (A) FLIM images depicting the long-lifetime fraction from measurements of mTurquoise2 in a U2OS cell. Photons were pooled from pixels grouped using boxcar windowing into groups of either 3×3 , 7×7 , or 11×11 pixels and analyzed using either the Bayesian analysis presented here, or least-squares fitting. (B) Histograms showing the probability density of the long-lifetime fraction from images in (A). The probability density functions from Bayesian analysis were

found to have mean values of 0.648 ± 0.069 , 0.642 ± 0.037 , and 0.640 ± 0.026 (mean \pm s.d.) for 3×3 , 7×7 , and 11×11 binning respectively, while the mean values were found to be 0.558 ± 0.137 , 0.648 ± 0.050 , and 0.652 ± 0.034 (mean \pm s.d.) for 3×3 , 7×7 , and 11×11 binning respectively using least-squares-fitting.

Figure 3.1: Schematic representation of the assumed conditions for FRET. Some tubulin molecules are labeled with a donor fluorophore (blue), some are labeled with an acceptor fluorophore (red), and some are unlabeled (grey). We assume FRET only occurs between a donor-labeled tubulin molecule that is nearby an acceptor-labeled tubulin molecule in a microtubule, while tubulin molecules not incorporated in microtubules are not engaged in FRET.

Figure 3.2: Measuring FRET with FLIM. (A) Schematic diagram of excitation and relaxation pathways of the donor (blue) fluorophore. When a donor fluorophore absorbs an incoming photon, the fluorophore is raised into an excited state. The fluorophore relaxes back to the ground state by either emitting a photon or releasing heat. FRET introduces an additional non-radiative pathway for the fluorophore to relax. Thus, the average time the fluorophore spends in an excited state, referred to as the lifetime, is shorter when the fluorophore is engaged in FRET. (B) In purified solutions, in the absence of acceptor, fluorescence-lifetime is not significantly affected by polymerization. Histogram of photon arrival times from Atto-565 conjugated tubulin (donor-labeled tubulin) in taxol-assembled microtubules (red dots) and without taxol (blue dots). Bayesian analysis of these histograms, using a single exponential decay model, estimates the fluorescence-lifetimes (with taxol $3.45 \pm .04$ ns and without taxol $3.67 \pm .03$ ns) and provides the corresponding models (with taxol, red curve and without taxol, blue curve). (C) In purified solutions, taxol-induced microtubules formed in the absence of an acceptor (green) produce a photon arrival-time histogram that is a decaying exponential with a lifetime of ~ 4 ns. FRET happens in the presence of acceptor fluorophore (purple), which induces the addition of a short component with a ~ 1 ns lifetime.

Figure 3.3: Investigating the relationship between FRET fraction and intensity: (A) An intensity image of microtubule structures in extract (left), and corresponding FRET fraction map (right). (B) FRET-fraction vs. intensity from the data in A for individual pixels (small blue dots) and grouped pixels (black dots). Error bars are the standard deviation of the posterior distribution. The grouped pixels are well-fit by Eq. 3.2.3 (dark grey dashed line) with $P_f = 0.123 \pm 0.006$ and $\varepsilon N_{mon} = 22.0 \pm 2.7$, where error is the 95% confidence interval.

Figure 3.4: Fit parameters change as expected when varying acceptor concentration. (A) Intensity images (left) and FRET fraction maps (right) of taxol induced microtubules in Xenopus egg extracts with high (top) and low (bottom) acceptor concentrations. FRET fraction maps were sensitive to acceptor concentration while the intensity images showed no significant differences. (B) Colored Dots: FRET-fraction and intensity from the data in A for grouped pixels. Error bars are the standard deviation of the posterior distribution. The grouped pixels are well-fit by Eq. 3.2.3 (grey dashed lines) with $P_f = 0.107 \pm 0.004$, $\varepsilon N_{mon} = 20.7 \pm 3.5$ for $1.3 \mu\text{M}$ acceptor and $P_f = 0.058 \pm 0.004$, $\varepsilon N_{mon} = 16.4 \pm 5.6$ for $0.6 \mu\text{M}$ acceptor. Samples with more acceptor have a larger horizontal asymptote, leading to a larger P_f , the probability of FRET. Meanwhile, the x-intercept is unchanged, leading to εN_{mon} , the number of photons from donor in monomer, being unchanged. C) Black dots: P_f determined from model fitting as shown in B. Colored circles note the P_f values from best-fit of data from samples shown in A and B. Error bars are 95% confidence intervals. P_f increases linearly with

acceptor concentration (grey dashed line). D) Black dots: εN_{mon} , determined from model fitting as shown in B. Colored circles note the εN_{mon} values from best-fit of data from samples shown in A and B. Error bars are 95% confidence intervals. εN_{mon} remains unchanged when acceptor concentration is varied.

Figure 3.5: Fit parameters change as expected when varying acquisition time. (A) Intensity images and FRET fraction maps of taxol induced microtubules in *Xenopus* egg extracts acquired with a long (purple) and a short (green) acquisition time. Shorter acquisition times resulted in dimmer images but similar FRET fraction maps. (B) Colored Dots: FRET-fraction and intensity from the data in A for grouped pixels. Error bars are the standard deviation of the posterior distribution. The grouped pixels are well-fit by Eq. 3.2.3 (grey dashed line) with $P_f = 0.330 \pm 0.012$, $\varepsilon N_{mon} = 76.4 \pm 3.5$ for 50 second acquisition and $P_f = 0.313 \pm 0.031$, $\varepsilon N_{mon} = 14.8 \pm 1.9$ for 10 second acquisition. The x-intercept increases with acquisition time, leading to a larger εN_{mon} . Meanwhile, the horizontal asymptote, which determines P_f , remains unchanged. C) Black dots: P_f , determined from model fitting as shown in B. Colored circles note the P_f values from best-fit of data from samples shown in A and B. Error bars are 95% confidence intervals. P_f remains unchanged when acquisition time is varied (grey dashed line). D) Black dots: εN_{mon} , determined from model fitting as shown in B. Colored circles note the εN_{mon} values from best-fit of data from samples shown in A and B. Error bars are 95% confidence intervals. εN_{mon} increases linearly with acquisition time (grey dashed line).

Figure 3.6: Microtubule dilution series to test measurements of polymer concentration. Polymer measurements by FRET-intensity (green dots) and centrifugation followed by absorption at 280 nm (blue dots) correspond to the expected polymer amount (black dashed line). Error bars are standard error of the mean. (Inset) Map of the concentration of tubulin subunits in polymer. Scale bar, 25 μm .

Figure 3.7: Investigating the relationship between FRET fraction and intensity in U2OS cells: (A) An intensity image of a mitotic spindle from a cell with both donor- and acceptor-labeled tubulin (top) and from a cell with only donor-labeled tubulin (bottom). (B) Colored Dots: FRET-fraction and intensity from the data in A for grouped pixels. Error bars are the standard deviation of the posterior distribution. The grouped pixels from the sample with both donor and acceptor is well-fit by Eq. 3.2.3 (grey dashed lines) with $P_f = 0.091 \pm 0.008$ and $\varepsilon N_{mon} = 19.9 \pm 4.6$, where error is the 68% confidence interval.

Figure 4.1: Schematic representation of two extreme models of nucleation. In the *all nucleation* model, nucleator activity is not affected by other microtubules. In the *bound nucleation* model, nucleators can only nucleate when bound to microtubules.

Figure 4.2: Schematic representation of nucleators diffusing away from the spindle boundary. (Top) In the *all nucleation* model, nucleators continue to create polymer as they diffuse away from the spindle. This predicts a gradient in polymer concentration. (Bottom) In the *bound nucleation* model, there is no gradient in the polymer concentration away from the spindle boundary.

Figure 4.3: FLIM measurements of FRET reveal polymer fraction. Tubulin in microtubules can FRET, which produce photons with a short lifetime. Soluble tubulin cannot FRET, and produce photons with a long lifetime. FLIM histograms can therefore be used to measure the fraction of tubulin in polymer.

Figure 4.4: Polymer concentration versus distance shows no significant angle dependence. (Left) Intensity images of spindles. Pixels are segmented into groups by their minimum distance from the spindle boundary in an angle dependent fashion. Grouping of pixels at a negative distance (green), small positive distance (orange), and large positive distance. (Middle) FRET fraction (blue) and intensity are measured in each pixel group to give a FRET versus distance and intensity versus distance graph. The grouping shown in (left) are denoted by dashed lines in the graph. (Right) Using the FRET and intensity data in (middle), polymer concentration versus distance is calculated. The grouping shown in (left) are denoted by dashed lines in the graph.

Figure 4.5: Polymer measurements of spindles are similar. The spindle boundary is overlaid in yellow over the spindle. No obvious $\sim 10\mu\text{m}$ gradient can be seen in any of the measurements.

Figure 4.6: The mean FRET fraction, intensity, and polymer concentration of 12 spindles show no obvious gradient in diffusible polymer. (Left) FRET fraction (blue) and intensity (red). Error bars are standard deviation of the posterior distribution of FRET fraction. (Right) Normalized polymer concentration reveals no $\sim 10\mu\text{m}$ gradient.

Figure 4.7: Low magnification imaging reveals the lack of a $100\mu\text{m}$ length scale gradient in polymer concentration. (A) FRET fraction and intensity measurements. (B) Using the FRET fraction and intensity data in (A), polymer concentration is calculated at each location to obtain a polymer versus distance curve. No long length scale ($20\text{-}200\mu\text{m}$) gradient in polymer concentration is observed.

Figure 4.8: The data supports the *bound nucleation* model while strongly arguing against the *all nucleation* model. The *bound nucleation* (blue dashed line) model predicts a sharp ($\sim 2\mu\text{m}$) gradient in polymer concentration, while the *all nucleation* model (green dashed line) predicts a long ($\sim 10\mu\text{m}$) gradient in polymer concentration. Polymer concentrations from 12 spindles are shown with grey lines. 1 and 2 standard deviations of these curves are shown in dark grey and light grey, respectively.

Figure S2.1. Posterior distributions generated using grid points and stochastic optimization are equivalent. Results from Markov chain Monte Carlo (red) and grid points (blue) were generated from the same data set.

Supplemental Figure S3.1: An intensity image (left) and corresponding FRET fraction map (right) when donor and acceptor labeled tubulin is added to *Xenopus* egg extract without inducing microtubule formation.

Dedicated to my mother, father, and grandfather.

ACKNOWLEDGEMENTS

In alphabetical order by first name:

Alex Fang

Alex Wolfe

Bryan Hassel

Che-Hang Yu

Dan Needleman

Dan Walsh

Emily Davis

Francis Costanzo

Jacky Austermann

Jan Brugués

Jason Kaye

Jess Crossno

Kelly Miller

Lukas Bane

Olivia Steihl

Paul Hansma

Peter Foster

Tae Yoo Yoen

Zain Ali

CONTRIBUTING SCIENTISTS

Chapter 2

Peter Foster, Tae Yoo Yeon, Daniel Needleman

Chapter 3

Tae Yoo Yeon, Peter Foster, Che-Hang Yu, Daniel Needleman

Chapter 4

Sebastian Fürthauer, Olivia Steihl, Peter Foster, Daniel Needleman

1

INTRODUCTION

Every person starts life as a single cell and through many cell divisions becomes composed of approximately 100 trillion cells. Every time a cell divides, the spindle self-assembles and brings half the chromosomes to each daughter cell. The spindle is a structure composed primarily of polymers called microtubules, and microtubules are composed of the protein tubulin. Microtubule activity can be divided into three categories:

- 1) Nucleation: the creation of new microtubules.
- 2) Dynamics: the growing and shrinking of microtubules.
- 3) Interactions: how microtubules move relative to each other.

Microtubule dynamics has been extensively studied and is relatively well understood. Microtubules are polar filaments, with a minus and plus end. In 1974, Allen and Borisy found that nearly all microtubule growth was at the plus end of the filament. A decade later, Mitchison and Kirchner showed that, in purified solutions, this plus end goes through stages of slow growth followed by rapid depolymerization, called catastrophe, until the microtubule has completely depolymerized (1984). In the mitotic spindle, FRAP has been used to show that microtubules turn over on the time scale of tens of seconds (Inoue and Sato, 1967; Salmon et al., 1984). In 2010, Needleman et al. used single-molecule speckle microscopy to measure how long a tubulin subunit resides in a microtubule before that subunit rejoins the monomer pool. Analysis of these measurements revealed that the average lifetime, the amount of time a microtubule exists before being depolymerized, is 20 seconds, and that the lifetime, growth velocity, and catastrophe rate are not spatially dependent within the spindle or outside of the spindle.

Microtubule interactions, mediated by cross-linking and motor proteins, has been extensively studied (Gatlin et al., 2009; Heald et al., 1996; Sawin et al., 1992; Merdes et al., 2000; Gaetz and Kapoor, 2004). Brugués et al. used laser ablation to measure the length distribution of microtubules throughout the spindle and infer the transport and local sorting of microtubules in the spindle (2012). Utilizing this information, Brugués et al. created a continuum model of the spindle, which described the spatial-temporal microtubule density and orientation fluctuations (2014). These fluctuations are well-explained by the local, mutual interactions of microtubules sliding and orienting each other, while polymerizing and depolymerizing. This produced strong evidence against a spindle matrix or other theories that imply long range interactions between microtubules.

In comparison to microtubule dynamics and interactions, microtubule nucleation is poorly understood. It is very difficult to directly measure nucleation. In purified solutions, nucleation is often studied by suddenly initiating polymer formation and measuring the subsequent amount of polymer formed as a function of time. This polymer versus time measurement is called a polymerization curve (Tobacman and Korn, 1983; Sept and McCammon, 2001). A typical polymerization curve starts with a lag phase wherein very little polymer forms, followed by an elongation phase, in which the mass of polymer rapidly increases and ends in a steady-state phase, wherein the total amount of polymer remains constant, even though individual filaments may dynamically grow and shrink (Flyvbjerg et al., 1996; Frieden, 1983; Cooper et al., 1983, Tobacman and Korn 1983). Analyzing these curves can reveal detailed information on the mechanisms of nucleation and growth. For instance, the duration of the lag phase is related to the rate of nucleation. Determining the dependence of the duration of the lag phase on subunit concentration allows inferences of the size of the critical nucleus (Zlotnick et al., 1999; Flyvbjerg et al., 1996; Wegner and Engel, 1975; Frieden and Goddette, 1983). Using light scattering to measure polymerization curves, microtubule formation was found to occur in 2/4/5 steps with a critical nucleus of 10/15/18 subunits, respectively, from three different studies (Voter and Erickson, 1984; Flyvbjerg et al., 1996; Flyvbjerg et al., 1997). Glycerol was used to induce microtubule formation, which may affect the critical nucleus size and the pathway of nucleation. Fygenson et al. measured microtubule formation in the absence of glycerol, in a much lower tubulin concentration regime, using fluorescence microscopy (1995). Their results suggest that there is a single stable state with critical size of 10-14 subunits. It remains unclear if microtubules in cells follow any of the pathways described above. In cells, microtubules are nucleated via microtubule nucleators, accessory proteins which greatly increase the rate of nucleation. Understanding how these proteins are regulated is crucial for understanding microtubule nucleation.

In cells, the first described and best understood mechanism for microtubule nucleation was from centrosomes (Brinkley, 1985) via gamma-tubulin ring complexes, γ TuRC (Keating and Borisy, 2000; Kollman et al., 2010; Moritz et al., 2000). However, spindle microtubules do not always rely upon centrosomes as plant cell mitosis and animal cell meiosis occur without centrosomes (Dumont and Desai, 2012; Zhang and Dawe, 2011) and animal cell mitosis can occur after centrosomes have been removed (Khodjakov et al., 2000; Megraw et al., 2001). While chromosomes are required for non-centrosomal microtubule nucleation, microtubules are nucleated throughout the body of the spindle (Brugués et al., 2012; Mahoney et al., 2006). The hypothesis that nucleation is affected by other microtubules in the spindle originated from observations that γ TuRC localized throughout the spindle (Lüders et al., 2005). There has been a great deal of research investigating microtubule-based microtubule nucleation. Petry et al. found that proteins involved in nucleation can bind to microtubules and facilitate the nucleation of microtubules (2013). While there have been many studies that tried to elucidate the specifics of microtubule-mediated microtubule nucleation (Petry et al., 2013; Kamasaki et al., 2013; Hsia et al., 2014; Ho et al., 2011; Wieczorek et al., 2015; Roll-Mecak et al., 2006), the most basic question remains unanswered: do microtubules simply localize nucleators, or do microtubules mediate the localization and activity of nucleators? In other words, is the activity of a nucleator affected by binding to a microtubule?

One reason this question has been challenging to address is that there is no direct way to measure nucleation in cells or cell extracts (Chapter 3, Introduction). Since I want to address this question, I will first have to build a method to measure nucleation. I will develop a novel Bayesian analysis of Fluorescence Lifetime Data to measure FRET (Chapter 2). I will then construct a FRET system to measure the amount of tubulin in polymer (Chapter 3). By studying the amount of polymer inside

and outside the spindle, I will investigate whether nucleators that leave the spindle, and are presumably not attached to microtubules, can still form polymer (Chapter 4).

2

DEVELOPING AND TESTING A BAYESIAN ANALYSIS OF FLUORESCENCE LIFETIME MEASUREMENTS

This chapter details and largely reproduces work previously published as Kaye B, Foster PJ, Yoo TY, Needleman DJ (2017). Developing and testing a Bayesian analysis of fluorescence lifetime measurements. PLOS ONE 12, e0169337.

ABSTRACT

FRET measurements can provide dynamic spatial information on length scales smaller than the diffraction limit of light. Several methods exist to measure FRET between fluorophores, including Fluorescence Lifetime Imaging Microscopy (FLIM), which relies on the reduction of fluorescence lifetime when a fluorophore is undergoing FRET. FLIM measurements take the form of histograms of photon arrival times, containing contributions from a mixed population of fluorophores both undergoing and not undergoing FRET, with the measured distribution being a mixture of exponentials of different lifetimes. Here, we present an analysis method based on Bayesian inference that rigorously takes into account several experimental complications. We test the precision and accuracy of our analysis on controlled experimental data and verify that we can faithfully extract model parameters, both in the low- photon and low-fraction regimes.

INTRODUCTION

Förster resonance energy transfer, or FRET, is a fluorescence technique commonly used to access spatial information on length scales smaller than the diffraction limit of light (Roy et al., 2008). In standard fluorescence, illuminating light is used to excite a fluorophore into a higher energy state, and the fluorophore subsequently relaxes into its ground state either by emitting a photon or through a

non-radiative decay pathway. If another fluorophore is near, typically within 10 nm, the two fluorophores can interact through dipole-dipole interactions termed FRET. FRET confers an additional decay path where the excited fluorophore, termed the donor, can transfer its energy to the nearby, unexcited fluorophore, termed the acceptor, which can then release the energy as a photon or through non-radiative decay. As the emission spectra of commonly used donor and acceptor pairs are spectrally distinct, one common method of measuring the average FRET efficiency is to compare the relative intensities collected from the two channels. However, this method has drawbacks including spectral bleed-through and a sensitivity to changes in fluorophore concentration and excitation light intensity (Wallrabe and Perisamy, 2005).

As an alternative to using fluorescence intensity to quantify FRET, fluorescence lifetime imaging microscopy, or FLIM, can be used (Stachowiak et al., 2012; Peter et al., 2005; Yoo and Needleman, 2016; Hinde and Digman, 2013). FLIM is a general technique that allows changes in a fluorophore's local environment to be probed. While use of FLIM is not limited to measuring changes in FRET, it can be used in this context without some of the drawbacks of an intensity based measurement. In time-domain FLIM, a narrow pulse of light is used to excite fluorophores into an excited state. Fluorophores that decay from their excited states can do so by releasing a photon. A subset of the released photons are detected, and for each detected photon, the arrival time is measured relative to the excitation pulse. The amount of time fluorophores spend in their excited state depends on the number of decay paths available. Donor fluorophores are chosen such that when they decay from their excited states, they do so at a constant rate, leading to photon emission time distributions that are exponential with a single characteristic decay time. This characteristic decay time is known as the fluorescence lifetime and is typically on the order of nanoseconds. When donor fluorophores are undergoing FRET, they will spend, on average, a shorter amount of time in their excited states,

leading to a reduced lifetime and quantum efficiency (Lakowicz 2006). In a sample where only a fraction of donor fluorophores are undergoing FRET, the photon emission time distribution will be the sum of two exponentials with different lifetimes. By comparing the amplitudes of these two exponentials, the relative fraction of donors undergoing FRET can be measured. In practice, additional complications are present, including photons collected from spurious background and time delays introduced by the collection system itself. These effects must be accounted for to infer the relative amplitudes and lifetimes of the emitted photon distributions from the measured photon arrival time histograms. Several approaches have been used in order to estimate these parameters, including least-squares fitting (Chang et al., 2007), rapid lifetime determination (Sharman et al., 1999), phasor methods (Stingari et al., 2011; Colyer et al., 2012; Chen et al., 2015), and Bayesian approaches (Rowley et al., 2011), each with their own advantages and disadvantages.

Here we utilize and extend the Bayesian approach previously described (Rowley et al., 2011) to take into account biexponential decays and additional experimental factors and we test the performance of our method using experimental data.

MATERIALS AND METHODS

BAYESIAN FRAMEWORK

Our framework is based on a previously described Bayesian analysis approach for measuring lifetimes from FLIM data (Rowley et al., 2011). For an introductory overview of Bayesian analysis, we direct

the reader to (Sivia, 2011). Bayes' Law states that given a set of data, t , and a set of model parameters θ , then,

$$p(\theta|t) \propto p(t|\theta) \cdot p(\theta) \quad Eq. 2.1$$

where $p(\theta|t)$, the probability of the model parameters given the measured data, is referred to as the posterior distribution, $p(t|\theta)$ is referred to as the likelihood function, and $p(\theta)$ is referred to as the prior distribution. The aim of Bayesian inference approaches is to find the posterior distribution for the given model and data, and hence what the probability is for each possible set of model parameters θ .

In time-domain FLIM measurements, a narrow laser pulse is used to excite fluorophores in the sample, and the arrival times of photons emitted from the fluorophores are recorded. Fluorophores undergoing FRET will have a shorter fluorescence lifetime compared with fluorophores not undergoing FRET. When only a fraction of fluorophores in the sample are undergoing FRET, the resulting distribution of photon emission will be a sum of exponentials, where each exponential has a different lifetime, and each exponential is weighted by the number of photons collected from the respective source. In addition, there exists a constant background of photons due to noise in the detector and stray light, taken to be from a uniform distribution. In the following, we consider photons from each of these sources separately and construct the likelihood function as follows,

$$p(\theta|t) \propto f_s \cdot p_s(t|f_s, \tau_s) + f_l \cdot p_l(t|f_l, \tau_l) + f_B \cdot p_B(t|f_B, \tau_B) \quad Eq. 2.2$$

where t is the arrival time of a photon relative to the excitation pulse, τ_s and τ_l are respectively the

short and long fluorescence lifetimes, f_s and f_l are the fractions of photons from the short and long lifetime distributions respectively, f_B is the fraction of photons from the uniform background given by $f_B = (1 - f_s - f_l)$. Here $p_i(t | f_i, \tau_i)$ is the probability of the photon arriving at time t given that the photon originates from fraction f_i .

Eq. 2.2 represents the likelihood model when time is taken to be continuous. However, in practice, photon arrival times collected with TCSPC are discretized into bins, and this discretization must be taken into account. If the bins are numbered sequentially and of width Δt , such that b_i represents the bin containing photons with arrival time, $(i - 1)\Delta t \leq t \leq i\Delta t$, then the likelihood function becomes,

$$p(\theta | t) = \prod_{i=1}^N [f_s \cdot p_s(t \in b_i | f_s, \tau_s) + f_l \cdot p_l(t \in b_i | f_l, \tau_l) \\ + f_B \cdot p_B(t \in b_i | f_B)]^{P_j} \quad Eq. 2.3$$

Thus, Eq. 2.3 serves as the discrete form of the likelihood function, Eq. 2.2.

INSTRUMENT RESPONSE FUNCTION

One complexity in experimental TCSPC measurements is that a delay is introduced to photon arrival times, termed the Instrument Response Function (IRF). In order to account for this effect, the IRF was experimentally measured (see FLIM Measurements). The measured IRF is then convolved with the idealized probability density functions for the exponential distributions in order to construct the likelihood function. Taking this effect into account leads to,

$$p_j(t \in b_i | f_j, \tau_j) = p_{em,j}(t \in b_i | f_j, \tau_j) \otimes IRF(t) \quad Eq\ 2.4$$

where $p_{em,j}$ is the idealized exponential distribution, taken to be $\propto e^{-t/\tau_j}$, where $j \in \{s, l\}$ is an index labeling the exponential distribution and $IRF(t)$ is the experimentally measured instrument response function.

POSTERIOR DISTRIBUTION

Using Eq. 2.4 in Eq. 2.3 leads to the final form of our likelihood function,

$$p(t|\theta) = \prod_{i=1}^N [f_s \cdot p_{em,s}(t \in b_i | f_s, \tau_s) \otimes IRF(t) + f_l \cdot p_{em,l}(t \in b_i | f_l, \tau_l) \otimes IRF(t) + f_B \cdot p_{em,j}(t \in b_i | f_B)]^{P_j} \quad Eq.\ 1.5$$

For comparison with experiments using control dyes where the lifetimes of the two molecules are well characterized, we choose a prior distribution such that the distribution is uniform for the fractions in the domain $f_j \in [0,1]$ and τ_s and τ_l are set to the measured values for Coumarin 153 and Erythrosin B respectively. With this choice of prior, Eq 2.1 becomes,

$$p(\theta|t) \propto p(t|\theta) \quad Eq.\ 2.6$$

and hence our posterior distribution is proportional to our likelihood function in the constrained

parameter space. To build the posterior distribution, parameter space is searched by evaluating the likelihood function on a grid of uniform spacing. Alternatively, parameter space can be searched stochastically using the Markov chain Monte Carlo method, yielding equivalent results (Supplemental Figure 2.1).

EFFECTS OF PERIODIC EXCITATION

For a single exponential decay, the probability of measuring a photon at time t , given a decay lifetime, τ , is given by,

$$p_{em}(t|\tau) \propto e^{-t/\tau} \quad Eq. 2.7$$

Where τ is the lifetime of the fluorophore. In practice, many sequential excitation pulses are used, and it's possible that a fluorophore excited by a given pulse doesn't emit a photon until after a future pulse. Taking this effect into account for a single exponential decay leads to (Rowley et al., 2011),

$$p_{em}(t|\tau) \propto \sum_{k=0}^{\infty} e^{-\frac{t+kT}{\tau}} \quad Eq. 2.8$$

where T is the excitation pulse period and k is an index counting previous pulses. The sum is a geometric series, which converges to,

$$p_{em}(t|t, \tau) \propto \frac{e^{-\frac{t}{\tau}}}{1 - e^{-\frac{T}{\tau}}} \quad Eq. 2.9$$

Thus, accounting for periodic excitations leads to a prefactor $\frac{1}{1-e^{-T/\tau}}$, which for a given T and τ is

constant. As we treat exponentials from populations with short and long lifetimes separately, this factor can safely be absorbed into the normalization constant, leaving the probability distribution unchanged.

FLIM MEASUREMENTS

FLIM measurements were carried out on a Nikon Eclipse Ti microscope using two-photon excitation from a Ti:sapphire pulsed laser (Mai-Tai, Spectra-Physics, 865 nm or 950 nm wavelength, 80 MHz repetition rate, 70 fs pulse width), a commercial scanning system (DCS-120, Becker & Hickl), and hybrid detectors (HPM-100-40, Becker & Hickl). The excitation laser was collimated by a telescope assembly to avoid power loss at the XY galvanometric mirror scanner and to fully utilize the numerical aperture of a water-immersion objective (CFI Apo 40x WI, NA 1.25, Nikon). Fluorescence was imaged with a non-descanned detection scheme with a dichroic mirror (705 LP, Semrock) that was used to allow the excitation laser beam to excite the sample while allowing fluorescent light to pass into the detector path. A short-pass filter was used to further block the excitation laser beam (720 SP, Semrock) followed by an emission filter appropriate for Coumarin and Erythrosin B (550/88nm BP, Semrock, or 552/ 27nm BP, Semrock). A Becker & Hickl Simple-Tau 150 FLIM system was used for time correlated single photon counting (Becker, 2010). The instrument response function was acquired using second harmonic generation of a urea crystal (Becker 2010).

For the data shown in Figure 2.1, the TAC range was set to 7×10^{-8} with a Gain of 5, corresponding to a 14 ns maximum arrival time. The TAC offset was set to 6.27%. The TAC limit high and limit low were set to 5.88% and 77.25%, respectively, resulting in a 10 ns recording interval.

Erythrosin B and Coumarin 153 samples were prepared at 10 mM and 15 mM, respectively.

Lifetimes were measured and fixed at values of 3.921 ns and 0.453 ns for Coumarin 153 and Erythrosin B respectively.

For the data shown in Figure 2.2, the *TAC range* was set to 5×10^{-8} with a *Gain* of 5, corresponding to a 10 ns maximum arrival time. The TAC *limit high* and *limit low* were set to 95.29% and 5.88%, respectively, resulting in a 10 ns recording interval. Illumination intensity was set such that 2.5×10^5 photons per second were recorded at the photon detector. Lifetimes were measured and fixed at values of 4.03 ns and 0.48 ns for Coumarin 153 and Erythrosin B respectively.

For the data shown in Figure 2.3, all settings and parameters were the same as for Figure 2.1.

IN VIVO FLIM-FRET MEASUREMENT

U2OS cell line was maintained in Dulbecco's modified Eagle's medium (DMEM, Gibco), supplemented with 10% Fetal Bovine Serum (FBS, Gibco), and 50 IU/mL penicillin and 50 mg/ mL streptomycin (Gibco) at 37°C in a humidified atmosphere with 5% CO₂. Cells were seeded on a 25-mm diameter, #1.5-thickness, round coverglass coated with poly-D-lysine (GG-25- 1.5-pdl, neuVitro). Transient transfection of pCMV-mTurquoise2-GFP plasmid was done with TransIT-2020 (Mirus), and cells were imaged 24 hours later. During imaging, the cells were maintained at 37°C on a custom-built temperature controlled microscope chamber, while covered with 1.5 ml of imaging media and 2 ml of white mineral oil (VWR) to prevent evaporation. The excitation wavelength was 850 nm, and the emission filter was 470/40 (Chroma). The excitation laser power was adjusted to 4

mW. Becker and Hickl SPCM acquisition parameters were set to 10x zoom, 256×256 image pixels, 5 second integration, and 256 ADC resolution.

SOFTWARE IMPLEMENTATION

All algorithms were implemented in MATLAB. The code used is freely available on Github at <https://github.com/bryankaye1/bayesian-analysis-of-fluorescent-lifetime-data>. Posterior distributions were generated by evaluating the likelihood function in a grid space of parameter values and were marginalized before estimation of the mode and mean for each parameter.

R_{ESULTS}

In a sample where only a subset of fluorophores is undergoing FRET, photon emission distributions take the form of a biexponential distribution, with some fraction of the distribution consisting of photons from a short-lifetime exponential, another fraction consisting of photons from a long-lifetime exponential, and some fraction coming from a spurious background distribution. The goal of FLIM analysis is to infer the relative weights of these distributions, along with the lifetimes of the two exponential distributions, from the measured histogram of photon arrival times (Figure 2.1A). Here we apply an analysis based on Bayesian inference in order to infer the most likely set of parameters from experimentally measured data. The output of our algorithm is a posterior distribution, which gives the relative probability of measuring a given set of parameters (Figure 2.1B).

To characterize our approach, we test our analysis in both the low-photon and low-fraction regimes, representing two extremes where data may be collected.

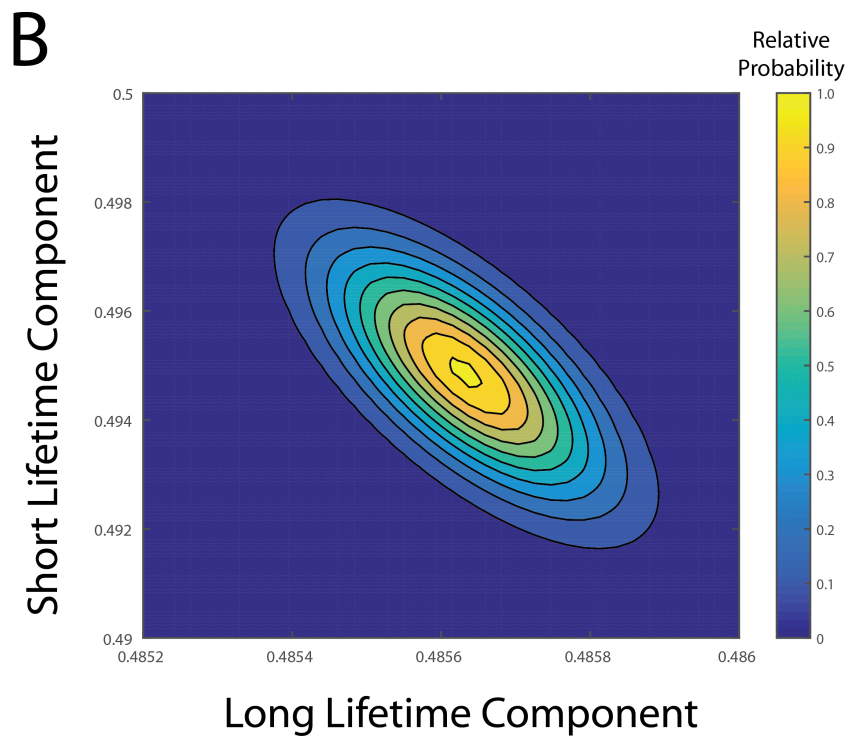
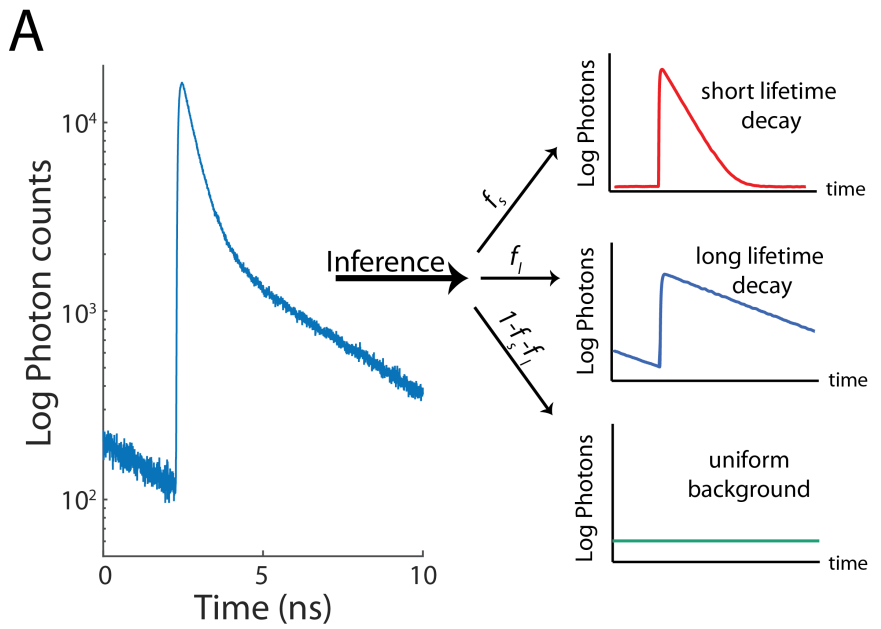


Figure 2.1. Photon arrival-time histograms are composed of the sum of two exponential distributions. (A) Photon arrival histogram composed of two exponential distributions, with a short-lifetime fraction f_s , a long-lifetime fraction f_l , and a background fraction $f_B = (1 - f_s - f_l)$ (B) Inferred posterior distribution generated from data in Fig 2.1A.

LOW-PHOTON REGIME

While the biexponential nature of FLIM histograms is apparent when the histogram is constructed using a large number of photons (Figure 2.1A), the histogram's underlying distribution is less obvious when the photon count is low (Figure 2.2A). Previous work has estimated the minimum number of photons necessary to achieve a certain accuracy in determining fluorescence lifetimes from TCSPC measurements (Köllner and Wolfrum, 1992). In this regime it can be difficult to extract accurate estimates of the fraction of short-lifetime photons through methods that rely on histogram fitting. This low-photon regime is relevant in many applications of FLIM, due to the fundamental tradeoff between the number of photons collected and both the spatial-temporal precision of the measurement and the light dose received by the sample. Thus, methods that can improve the precision and accuracy of parameter estimation in the low-photon count regime could potentially lead to a practical increase in spatial-temporal resolution and lower light doses.

In order to test the accuracy and sensitivity of our analysis, fluorescence lifetime measurements were taken using Erythrosin B and Coumarin 153, two reference dyes with well characterized lifetimes of 0.47 ± 0.02 ns and 4.3 ± 0.2 ns respectively (Boens et al, 2007). These dyes were mixed at a fixed ratio, and fluorescence lifetime measurements were taken (Figure 2.2A, Materials and Methods) in order to generate a master list of photon arrival times. A fixed number of photons were randomly sampled from the master list in order to construct a histogram of photon arrival times, and analyzed to infer an estimate of the fraction of short-lifetime fluorophores, f_s , taken as either the mean or the mode of the posterior distribution, while the known lifetimes were held fixed (Materials and Methods). This process was repeated 300 times in order to produce an error estimate for each given

photon count, and was repeated for total photon counts spanning 3 orders of magnitude (Figure 2.2B).

We find good agreement between the estimates of the fraction of short-lifetime photons for total photons counts larger than 200 photons, using either the posterior mean or posterior mode as a fraction estimate (Figure 2.2B). Slight discrepancies between estimates using the posterior mean and posterior mode are apparent due to truncation and the fact that the posterior distribution is skewed (Figure 2.1B), and thus in general the mode and the mean of the distribution are not equal. As a measure of the error in our parameter estimation, we compute the standard deviation of the estimates from the 300 numerical replicates (Figure 2.2C) for each photon count.

Fitting a power law to all data points except for the four smallest photon counts yields an exponent of -0.48 ± 0.04 (95% confidence interval), consistent with the exponent of -0.5 predicted from the central limit theorem in the limit of high n_{photons} . This $\sqrt{n_{\text{photons}}}$ scaling is also evident for other analysis methods, including the rapid lifetime determination method (Sharman et al., 1999), which has comparable error for high n_{photons} .

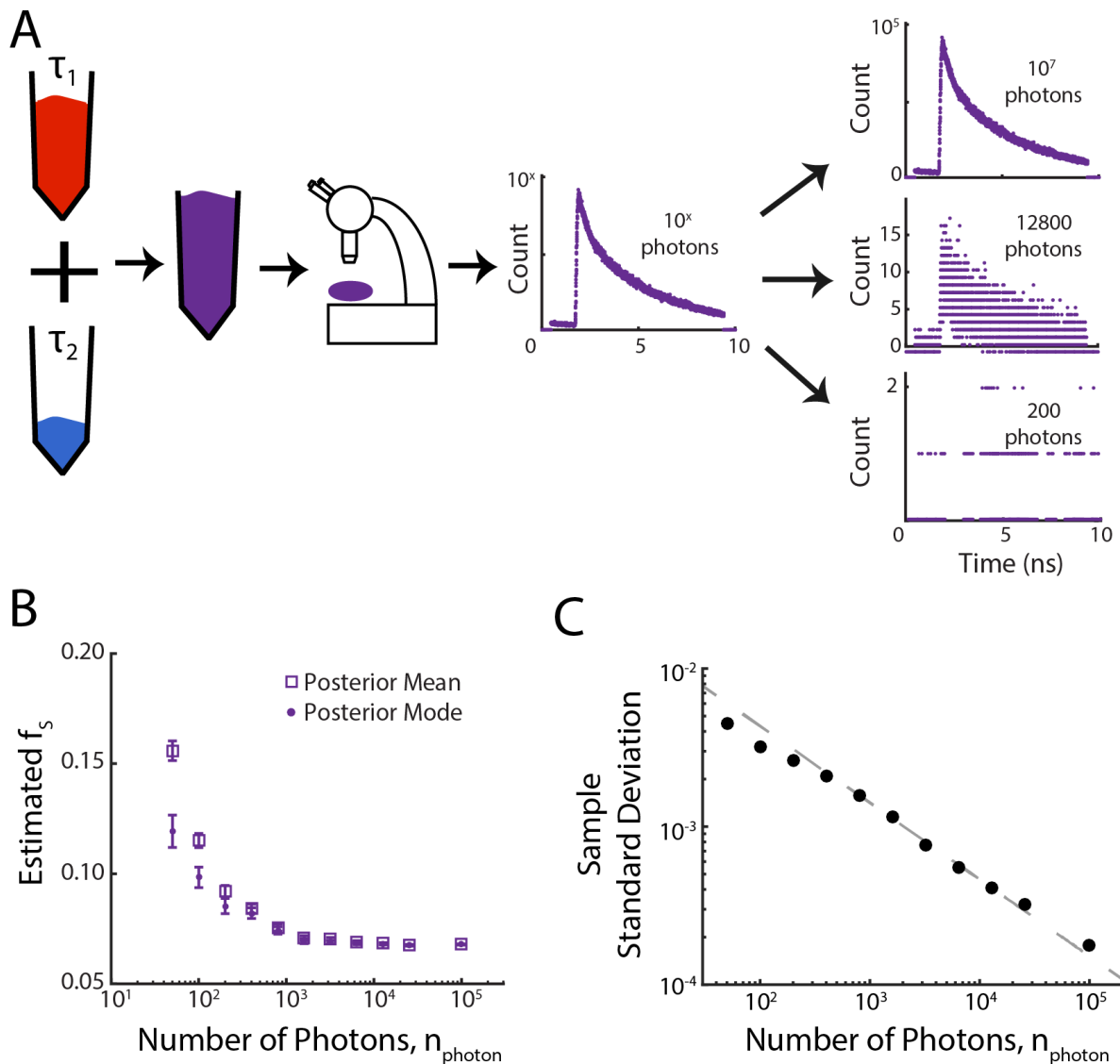


Figure 2.2. Low-Photon Regime. (A) Control dyes having known long (Coumarin 153) and short (Erythrosin B) lifetimes were mixed at a fixed ratio. From the measured master curve of photon arrival times, a variable number of photons are randomly sampled, generating histograms with a variable number of photons. (B) Bias in the estimated short-life photon fraction, f_s , decreases with increasing photon number. Data points represent the average of the posterior mean (squares) or mode (circles) for 300 independent samplings for each photon count. Error bars are s.e.m. (C) Black circles: measured sample standard deviations from data in Fig 2B averaged across the 300 independent samplings. The sample standard deviation decreases approximately as n_{photon}^{-b} . Power law fit to $a \times x^b$ for all but the four lowest values of n_{photon} shown in gray, with $a = 0.04 \pm 0.01$ and $b = -0.48 \pm 0.04$ (95% confidence interval).

LOW-FRACTION REGIME

We next tested our results in the regime where a relatively large number of photons are collected, but the fraction of photons originating from the short-lifetime component is low. This regime is relevant in systems where a large number of donor molecules are present, but interactions leading to FRET are relatively rare. In order to test the performance of our algorithm in this regime, fluorescence lifetime measurements were taken of Erythrosin B and Coumarin 153 as representative short- and long-lifetime dyes respectively. Unlike the measurements taken in the low-photon regime, separate fluorescence lifetime measurements were taken for each dye, generating separate master photon histograms (Figure 2.3A). A fixed number of photons could then be numerically sampled from each master histogram in order to create test histograms containing a prescribed fraction of photons originating from the short-lifetime dye, which were then analyzed in order to estimate the short-lifetime fraction while the lifetimes were held fixed at their previously measured values (Materials and Methods). Data was collected at 1.5×10^5 , 1.2×10^6 , and 4.8×10^6 counts per second, corresponding to low, medium, and high intensity respectively, and histograms from each intensity were analyzed separately.

Photons were sampled from master curves such that the total number of photons was fixed at 5×10^7 , with a prescribed fraction of photons originating from the short-lifetime distribution. This process was repeated 100 times for each condition. Across orders of magnitude, the short-lifetime fraction estimated from our algorithm varies linearly with the prescribed short-lifetime fraction (Figure 2.3B), with linear fits giving slopes of 0.9933 ± 0.0026 , 1.0085 ± 0.0024 , and 1.0106 ± 0.0031 , and offsets of $0.002000 \pm 0.0484 \times 10^{-4}$, $0.004400 \pm 0.0814 \times 10^{-4}$, and $0.009500 \pm 0.1992 \times$

10^{-4} for low, medium, and high intensities respectively (95% confidence interval). The estimated short-lifetime fraction differs from the known short-lifetime fraction by a small bias factor, evident by the small positive offsets in the linear fits (Figure 2.3B, Inset). We hypothesize that this offset may be due to a number of factors, including non-monoexponential photon emission from the dyes, slight mischaracterization of the lifetimes or the instrument response function, or an intensity dependence of the FLIM measurement system. While the magnitude of the bias varies with intensity, the magnitude of the bias is relatively small, overestimating the fraction by less than one percent for the highest intensity tested.

In many applications, the changes in FRET fraction are more relevant than the actual fraction values themselves. Thus, we next considered the accuracy of measuring changes in the short-lifetime fraction, which were derived from the results in Figure 2.3B by subtracting values adjacent on the short-lifetime fraction axis. While the estimated short-lifetime fractions contain a small bias (Figure 2.3B), the bias is largely removed when changes in short-lifetime fraction are considered (Figure 2.3C). Consistent with this removal of bias, fitting linear equations to the estimated changes in short lifetime fraction vs. prescribed short lifetime fraction gives slopes of 0.9573 ± 0.1895 , 1.0013 ± 0.1445 , and 0.9580 ± 0.1717 , and offsets of $(0.2332 \pm 0.3712) \times 10^{-5}$, $(0.3215 \pm 0.3088) \times 10^{-5}$, and $(0.4617 \pm 0.4286) \times 10^{-5}$ for low, medium, and high intensities respectively (95% confidence interval) (Figure 2.3C). These results demonstrate the accuracy and precision of our method for measuring changes in short-lifetime fraction across many orders of magnitude. For a short-lifetime fraction of $2 \cdot 7$, the sample standard deviation decays with increasing photon number. Fitting a power law yields an exponent of -0.4764 ± 0.0471 (95% confidence interval), consistent with the exponent of -0.5 predicted from the central limit theorem and as was the case for the low-photon regime measurements (Figure 2.2C).

Figure 2.3. Low-fraction regime. (A) Samples of dyes with short-lifetime (Erythrosin B) and long-lifetime (Coumarin 153) were prepared, and fluorescence lifetime measurements were collected for each dye separately, leading to separate master photon histograms. Test histograms were constructed by randomly sampling a fixed number of photons, with varying fractions being drawn from the master lists of short-lifetime and long-lifetime photons. These histograms were then analyzed in order to estimate the fraction of short-lifetime photons, f_s . (B) The estimated short-lifetime fraction, f_s , varies linearly with the constructed short-lifetime fraction for three different total photon numbers, with a small offset. Squares: estimate from posterior mode. Dots: estimate from posterior mean. Dashed lines: linear fits with slopes 0.9933 ± 0.0026 , 1.0085 ± 0.0024 , and 1.0106 ± 0.0031 , and offsets of $0.002000 \pm 0.0484 \times 10^{-4}$, $0.004400 \pm 0.0814 \times 10^{-4}$, and $0.009500 \pm 0.1992 \times 10^{-4}$ for low, medium, and high intensities respectively (95% confidence interval). Intensities correspond to data collected at 1.5×10^5 , 1.2×10^6 , and 4.8×10^6 counts per second, for low, medium, and high intensity respectively. Inset: Data from main figure shown on a log-log scale. (C) Changes in the estimated short-lifetime fraction track the known changes in the short-lifetime fraction. Squares: estimate from posterior mode. Dots: estimate from posterior mean. Dashed lines: Linear fits with slopes of 0.9573 ± 0.1895 , 1.0013 ± 0.1445 , and 0.9580 ± 0.1717 , and offsets of $(0.2332 \pm 0.3712) \times 10^{-5}$, $(0.3215 \pm 0.3088) \times 10^{-5}$, and $(0.4617 \pm 0.4286) \times 10^{-5}$ for low, medium, and high intensities respectively (95% confidence interval).

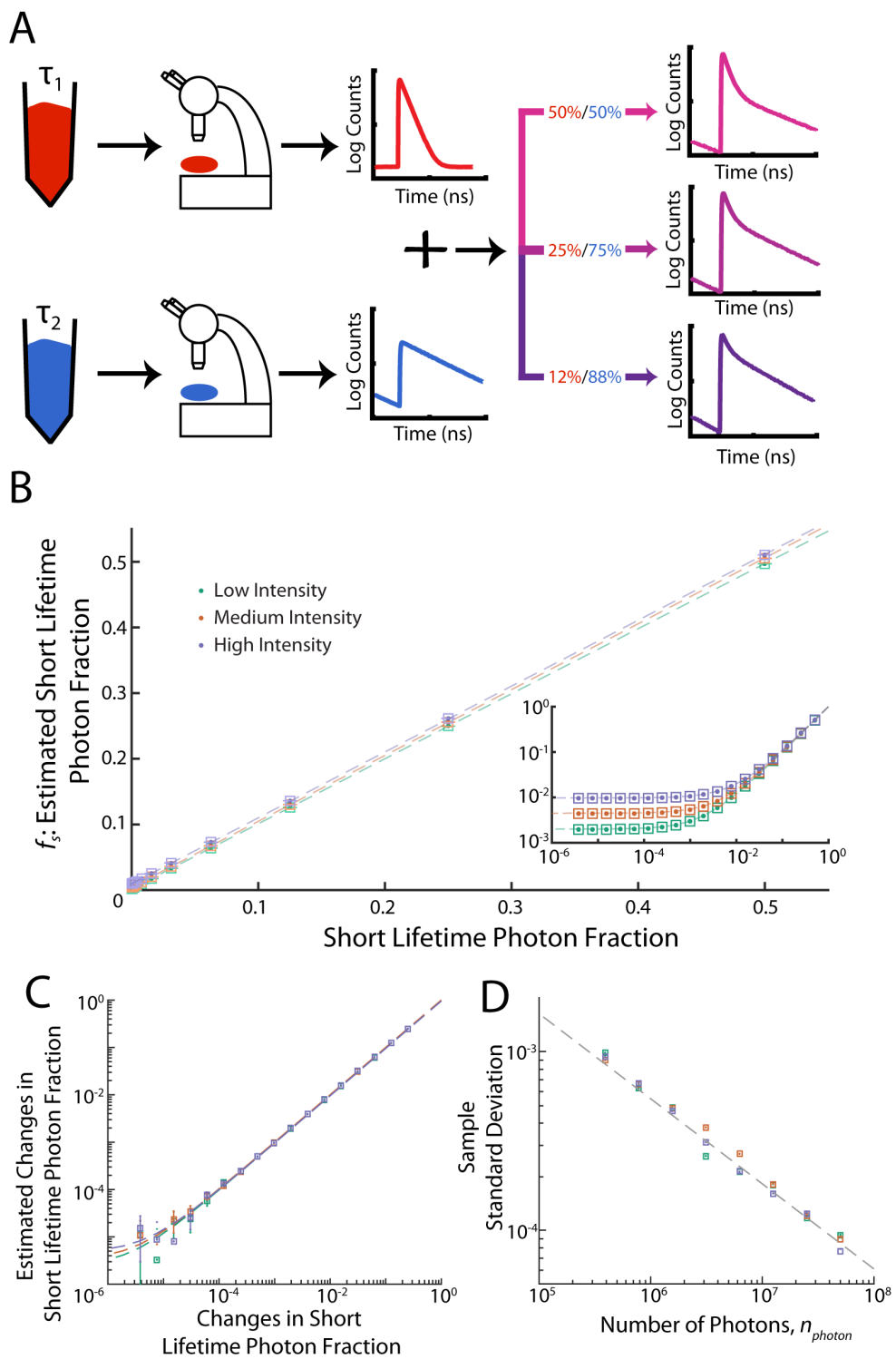


Figure 2.3 (Continued)

IN VIVO TESTING AND METHOD COMPARISON

As FLIM is commonly used to measure FRET in living systems between biological fluorophores, which may contain complications not accounted for in our model, we next tested the applicability of our method in living cells. FLIM measurements were carried out on U2OS cells transfected with a plasmid carrying mTurquoise2-4AA-GFP, a fusion between the FRET pair of mTurquoise2 and GFP (Figure 2.4A). As these two fluorophores are physically attached to each other in close proximity, a fraction of the donor mTurquoise2 molecules undergo FRET, and thus have a short lifetime. However, as these fluorophores must undergo maturation before being functional, some fraction of mTurquoise2 molecules will be attached to GFP that are not fully mature and thus will not undergo FRET, leading to a long-lifetime fraction.

To test the performance of our method as a function of the photon number, photon arrival times were pooled within the cell using boxcar windowing, from areas of either 3×3 , 7×7 , or 11×11 pixels corresponding to average photon counts of $1,087 \pm 260$, $5,826 \pm 1,451$, and $14,105 \pm 3,673$, respectively (Figure 2.4B). In order to more readily make comparisons with the least-squares method, we here infer the relative amplitudes of the biexponential decay, instead of the relative photon populations previously considered, and thus consider the long-lifetime amplitude fraction instead of the long-lifetime photon fraction considered above. Using the Bayesian method, the distributions of the long-lifetime fraction were found to have mean and standard deviation values of 0.648 ± 0.069 , 0.642 ± 0.037 , and 0.640 ± 0.026 (mean \pm s.d.) for 3×3 , 7×7 , and 11×11 binning respectively, showing little change for all conditions.

In order to compare the results from the Bayesian method presented here with the more commonly used least-squares fitting method, we repeated our analysis using fitting routines built into the Becker

& Hickl software (Figure 2.4A and 2.4B). Mean and standard deviation values of the long-lifetime fraction distributions were found to be 0.558 ± 0.137 , 0.648 ± 0.050 , and 0.652 ± 0.034 (mean \pm s.d.) for 3×3 , 7×7 , and 11×11 binning respectively. While the mean value for the long-lifetime fraction is similar for higher photon counts, there is significant discrepancy for 3×3 binning, where an asymmetric distribution is evident. Furthermore, for the highest photon counts, the mean values agree within error for the Bayesian method and least-squares fitting, indicating a convergence between the two methods in the limit of high photon number. Thus, for low-photon counts, the Bayesian method presented here provides long-lifetime fraction estimates that are more accurate and precise than the nonlinear least-squares method.

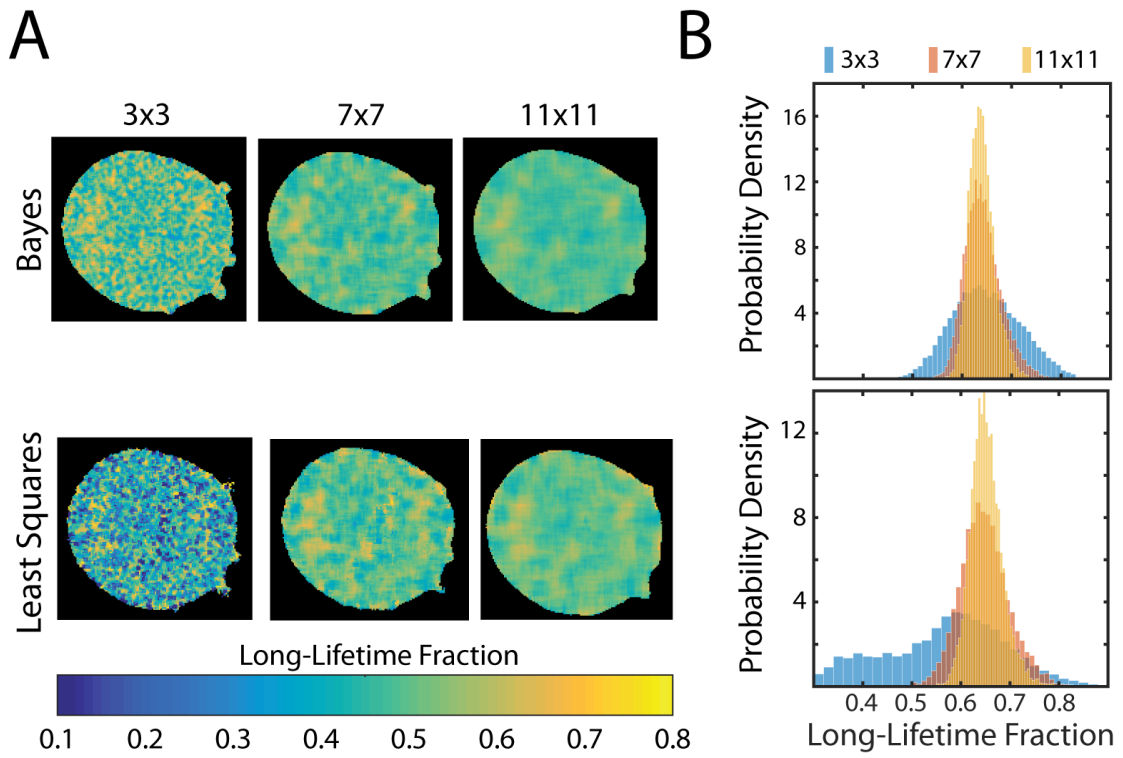


Figure 2.4. *In vivo* Testing. (A) FLIM images depicting the long-lifetime fraction from measurements of mTurquoise2 in a U2OS cell. Photons were pooled from pixels grouped using boxcar windowing into groups of either 3×3 , 7×7 , or 11×11 pixels and analyzed using either the Bayesian analysis presented here, or least-squares fitting. (B) Histograms showing the probability density of the long-lifetime fraction from images in (A). The probability density functions from Bayesian analysis were found to have mean values of 0.648 ± 0.069 , 0.642 ± 0.037 , and 0.640 ± 0.026 (mean \pm s.d.) for 3×3 , 7×7 , and 11×11 binning respectively, while the mean values were found to be 0.558 ± 0.137 , 0.648 ± 0.050 , and 0.652 ± 0.034 (mean \pm s.d.) for 3×3 , 7×7 , and 11×11 binning respectively using least-squares-fitting.

DISCUSSION

Here we presented an extension of previous Bayesian inference approaches to FLIM data analysis that takes into account additional experimental complexities. Using controlled experimental data as a test case, we show that this analysis performs remarkably well in both the low- photon and low-

fraction regimes.

In the low-photon regime, we can estimate the low-lifetime fraction, f_s , with a precision of 0.003 and a bias of 0.017 using only 200 photons. At a photon collection rate of 2×10^5 photons per second, this number of photons corresponds to an acquisition time of only 1 millisecond. As the precision scales as $n_{\text{photon}}^{-1/2}$ (Figure 2.2C), if one instead wanted a higher precision of 0.001, one could instead collect data for 9 milliseconds. In the low-fraction regime, using 5×10^7 photons, for a short-lifetime fraction, f_s , of 0.0156, we find a precision of 0.000096 and a bias of 0.0046. With an acquisition rate of 1.5×10^6 photons per second, this corresponds to 33 seconds of acquisition time. As the precision in this regime also scales as $n_{\text{photon}}^{-1/2}$ (Figure 2.3C), if one requires a higher precision of 0.000032, this could be obtained by acquiring data for nine times as long, or 300 seconds. Thus, in both the low-photon and low-fraction regimes, our results show the required number of photons, and hence the acquisition time, necessary to achieve a given level of precision.

One limitation of our implementation is that we evaluate the posterior distribution at equally spaced points. A large parameter space must be searched, and the analysis presented here is relatively slow compared to other parameter searching techniques. For example, when 4 parameters are searched using a Markov chain Monte Carlo approach to stochastically optimize our likelihood, the computation time is reduced by a factor of 10-20 with no loss of accuracy (Figure S2.1).

Here we have focused on the use of FLIM to measure changes in FRET, yet it has wider applications, including in metabolic imaging (Bird et al., 2005) and in measuring local changes in environment, including pH (Lin et al., 2003) as well as oxygen (Gerritsen et al., 1997) and Zn^{2+} (Ripoll et al., 2015) concentrations. The analysis presented here is general, and should be applicable to FLIM measurements in these other systems as well.

3

BRIDGING LENGTH SCALES TO MEASURE POLYMER ASSEMBLY

This chapter details and largely reproduces work previously published as Kaye B, Yoo TY, Foster PJ, Yu C, Needleman DJ (2017). Bridging length scales to measure polymer assembly. Molecular Biology of the Cell.

ABSTRACT

Time-resolvable quantitative measurements of polymer concentration are very useful to elucidate protein polymerization pathways. There are numerous techniques to measure polymer concentrations in purified protein solutions, but few are applicable *in vivo*. Here we develop a methodology combining microscopy and spectroscopy to overcome the limitations of both approaches for measuring polymer concentration in cells and cell extracts. This technique is based on quantifying the relationship between microscopy and spectroscopy measurements at many locations. We apply this methodology to measure microtubule assembly in tissue culture cells and *Xenopus* egg extracts using two-photon microscopy with FLIM measurements of FRET. We find that the relationship between FRET and two-photon intensity quantitatively agrees with predictions. Furthermore, FRET and intensity measurements change as expected with changes in acquisition time, labeling ratios, and polymer concentration. Taken together, these results demonstrate that this approach can quantitatively measure microtubule assembly in complex environments. This methodology should be broadly useful for studying microtubule nucleation and assembly pathways of other polymers.

INTRODUCTION

Many proteins assemble into polymers, including cytoskeletal proteins (Desai and Mitchison, 1997; Fletcher and Mullins, 2010; Oosawa and Kasai, 1962), metabolic proteins (O'Connell et al., 2012;

Petrovska et al., 2014), virus capsid proteins (Dokland, 2000; Katen and Zlotnick, 2009), and proteins involved in DNA replication, repair, and recombination (Meyer and Laine, 1990; Cox, 2001).

Therefore, understanding the mechanism of polymer assembly, and its regulation and consequences is crucial for understanding a wide variety of biological processes.

Polymer assembly can be divided into two processes: nucleation, the creation of a new polymer from its constituent subunits; and growth, the further polymerization of an already formed polymer (Dokland, 2000; Katen and Zlotnick, 2009; Flyvbjerg et al., 1996; Frieden, 1985; Pollard, 1990; Desai and Mitchison, 1997). Nucleation and growth are both typically regulated by accessory proteins.

Polymer assembly is often studied in *in vitro* solutions of purified subunits by suddenly initiating polymer formation and measuring the subsequent amount of polymer formed as a function of time (Flyvbjerg, 1996; Frieden, 1983; Cooper et al., 1983; Zlotnik et al., 1999). Such a time-course measurement is referred to as a polymerization curve (Tobacman and Korn, 1983; Sept and McCammon, 2001). A typical polymerization curve contains an initial lag phase, in which very little polymer forms, followed by an elongation phase, in which the mass of polymer rapidly increases, and finally, a steady-state phase, wherein the total amount of polymer remains constant, even though individual filaments may dynamically grow and shrink (Flyvbjerg et al., 1996; Frieden, 1983; Cooper et al., 1983; Tobacman and Korn 1983). Polymerization curves can be used to obtain detailed information on the mechanisms of nucleation and growth, and their regulation by accessory proteins. For example, the duration of the lag phase is related to the rate of nucleation. Determining the dependence of the duration of the lag phase on subunit concentration allows inferences of the size of the critical nucleus (Zlotnick et al., 1999; Flyvbjerg et al., 1996; Wegner and Engel, 1975; Frieden and Goddette, 1983). Furthermore, an accessory protein whose addition causes a reduction in the lag phase can be concluded to facilitate nucleation.

To obtain polymerization curves, it is necessary to use an experimental technique that can quantitatively measure the concentration of polymer over time. A variety of such techniques are available for *in vitro* systems, but there is a lack of techniques that can be applied *in vivo*. Light scattering and small-angle x-ray scattering have been widely used to measure polymerization curves of purified components (Wegner and Engel, 1975; Voter and Erikson, 1984; Bordas et al., 1983; Matsudaira et al., 1987). These techniques are confounded in cells and cell extracts by the presence of numerous other scatterers besides the protein polymer of interest. Biochemical assays, such as centrifugation and gel filtration, can be used to measure polymer amount *in vivo*, but these methods are not suitable for obtaining polymerization curves because they are destructive and often have a temporal resolution that is too low to capture the dynamics of polymer assembly.

Fluorescence techniques can provide high temporal resolution and are non-destructive, but attempting to use them for quantitative measurements of polymer concentration *in vivo* poses several challenges. It is possible to divide fluorescence techniques into two broad categories: microscopy based techniques, which provide an image of the sample, and spectroscopy based techniques, which produce a signal based on the properties of the fluorophore, such as its brightness, emission spectrum, or polarization.

If microscopy were capable of visualizing and determining the length of every individual filament, then it could be used to directly measure the amount of protein in polymer. This is rarely possible in practice because of the finite resolution of light microscopy and the high background signal generated by soluble subunits. Microscopy can still be used to obtain information on polymer assembly because significant polymerization can result in visible inhomogeneity. For example,

microtubules organize into asters when assembled in cell extracts, and thus the presence of asters has been used as an assay to study factors that influence microtubule assembly (Helmke and Heald, 2014; Wiese et al., 2001; Ohba et al., 1999). It is challenging to use such an assay to quantitatively measure polymer concentration because the presence of asters, and other large structures that can be easily visualized, depends on microtubule interactions in addition to microtubule assembly. Another difficulty is that the background signal from soluble subunits must be accounted for when using microscopy to measure polymer concentration. If the soluble subunits are assumed to be spatially uniform, then a simple background subtraction is sufficient, but it is often unclear how to test the validity of that assumption. Even if it can be confirmed that the soluble subunit concentration is uniform, estimating the resulting background intensity for all the time points of a polymerization curve can be difficult in practice, especially in the absence of resolvable structures.

Fluorescence spectroscopy techniques are based on the use of a probe that changes its fluorescence properties upon protein polymerization. Pyrene conjugated to actin, which undergoes an ~10-fold increase in brightness upon actin polymerization (Cooper 1982), has been extensively used to obtain actin polymerization curves *in vitro* (Tellam and Friedan, 1982; Pollard and Cooper, 1986; Mullins et al., 1998; Rohatgi et al., 2001; Wen and Rubenstein, 2009). When two fluorophores are in close proximity, typically less than ~5 nm, energy can transfer between them through a non-radiative process called Förster Resonance Energy Transfer (FRET). Thus, if FRET between probes attached to subunits only occurs in polymer, measuring the change in the fluorescent properties associated with energy transfer can be used to measure polymer concentration. For example, FRET has been used to study actin (Wang and Taylor, 1981; Taylor et al., 1981; Okamoto and Hayashi 2006) and ParM (Garner et al., 2004) polymerization. While fluorescent spectroscopy has been used to study polymerization, it is challenging to quantitatively measure polymer concentration *in vivo* because the

fluorescent properties of probes can be strongly modified by changes in the local environment not associated with polymer assembly, such as the pH and interactions with ions, lipids, and other proteins. Furthermore, interpretation of spectroscopy data requires the use of models of how fluorescence properties change upon polymerization, which can be difficult to experimentally verify.

Here we present a methodology to bridge the large length scales accessible with microscopy and the small length scales accessible with spectroscopy, and overcome the limitations of both approaches for measuring polymer concentration in cells and cell extracts. We show that simultaneously acquired microscopy and spectroscopy measurements can be used to cross-validate the models that underlie the interpretation of these techniques, thereby enabling quantitative measurements of polymer concentration. We apply this general approach to measure microtubule concentration in both *Xenopus laevis* oocyte extracts and U2OS cells by combining FRET and fluorescence microscopy. To measure FRET, we use a Bayesian analysis of fluorescence lifetime imaging microscopy data (Bastiaens and Squire, 1999; Becker, 2010; Kaye, Foster, Yoo et al., 2017; Rowley et al., 2011, Rowley et al., 2016), which accounts for statistical noise and imperfections in the measurement system. We find quantitative agreement between theory and experiment for the predicted relationship between spectroscopy and microscopy data, and the resulting variations with acquisition time, fluorophore labeling ratios, and microtubule concentration. This method should prove useful for studying the mechanism and regulation of microtubule nucleation. More broadly, combining spectroscopy and microscopy should provide a powerful tool for obtaining polymerization curves from a variety of polymers in cells and cell extracts.

R_ESULTS

ABSTRACT FORMALISM

We constructed an approach to cross-validate microscopy and spectroscopy signals that is applicable for many techniques. In this section, we present the abstract formalism. In the next section, we derive in detail how the approach applies to a specific pair of microscopy and spectroscopy techniques.

There are many properties of light that can be used as measurements of polymer concentration. We refer to these measurements as the *signal*. Most signals depend on both the amount of monomer and the amount of polymer. Since monomer assembles into polymer, the sum of the amount of monomer and polymer in the bulk does not change in time. Thus, if the signal is proportional to the sum of monomer and polymer, the spatial average of this signal will not change in time. We refer to this signal as the microscopy signal, since it relies upon comparing the signal at different locations to infer the polymer concentration in the sample. We refer to a signal that does not require spatial information to measure the polymer concentration as the spectroscopic signal.

Our approach requires two spatially resolvable measurements of polymer. While we assume one microscopy signal and one spectroscopic signal, this approach is unchanged if both signals are spectroscopic. Our method compares the microscopy and spectroscopy signals at many locations, i.e. pixels, to test the relationship between the signals. If the polymer amount is not spatially uniform, imaging an area with both the microscopy and spectroscopic signal allows for testing the relationship between both signals at many different polymer concentrations. In general, the spectroscopic signal,

\tilde{F} , and the microscopy signal, \tilde{I} , at a specific location x , will depend on the local number of subunits in monomer, $N_{mon}(x)$ the local number of subunits in polymer, $N_{pol}(x)$, and other global parameters, $\lambda_{\tilde{F}}$ and $\lambda_{\tilde{I}}$, that effect either the microscopy signal or the spectroscopic signal respectively:

$$\tilde{F} = \tilde{F}(N_{pol}(x), N_{mon}(x), \lambda_{\tilde{F}}) \quad (Eq. 3.1.1)$$

$$\tilde{I} = \tilde{I}(N_{pol}(x), N_{mon}(x), \lambda_{\tilde{I}}) \quad (Eq. 3.1.2)$$

Since both the microscopy and the spectroscopic measurement depend on the number of subunits in polymer, N_{pol} , it is possible to solve for N_{pol} in terms of \tilde{I} to construct a relationship between \tilde{F} and \tilde{I} (i.e. combine Eq. 3.1.1 and Eq. 3.1.2) to find:

$$\tilde{F} = \tilde{F}(\tilde{I}(x), N_{mon}(x), \lambda_{\tilde{F}}, \lambda_{\tilde{I}}) \quad (Eq. 3.1.3)$$

Eq. 3.1.3 quantitatively links two measured quantities, the spectroscopic signal and the microscopy signal, through the parameter of interest, N_{pol} . If the functional relationship between \tilde{F} and \tilde{I} is experimentally measured and found to follow the form predicted by Eq. 3.1.3, then both Eq. 3.1.1 and Eq. 3.1.2 would be validated. Since each pixel contains a measurement of the spectroscopic and microscopy signal, a single image produces many data points with which to test Eq. 3.1.3.

To calculate polymer amount at a specific location using both \tilde{F} and \tilde{I} , we combine Eq. 3.1.1 and Eq. 3.1.2 to write N_{pol} in terms of the \tilde{F} and \tilde{I} :

$$N_{pol} = N_{\square ol}(\tilde{F}(x), \tilde{I}(x), N_{mon}(x), \lambda_{\tilde{F}}, \lambda_{\tilde{I}}) \quad (Eq. 3.1.4)$$

We will apply this approach to construct a system for measuring the amount of tubulin in polymer in cell extracts. We use Fluorescence Lifetime Imaging Microscopy (FLIM) for our spectroscopic technique to measure FRET, our spectroscopic signal. We use two-photon imaging as our microscopy technique to measure fluorescence intensity, our microscopy signal. However, other microscopy or spectroscopy techniques could be used instead. In the next section, we present explicit models (i.e. write out the form of Eq. 3.1.1 and Eq. 3.1.2 for our system) to construct a relationship between FRET and fluorescence intensity (i.e. Eq. 3.1.3 for our system) and the relationship between these measurements and polymer amount (i.e. Eq. 3.1.4 for our system). Then in the following sections, we develop a quantitative means of measuring FRET using FLIM and we experimentally test the relationship between FRET and intensity in cell extracts. In the last section, we experimentally test how well our system measures the amount of tubulin in polymer in a purified system.

MODELING THE RELATIONSHIP BETWEEN FRET, FLUORESCENCE INTENSITY, AND POLYMER

In this section, we present a model that relates the amount of tubulin assembled into microtubules to FRET and fluorescence intensity. We make several assumptions in the construction of the model, the validity of which will be tested based on the applicability of the model's predictions to experimental data. We consider a scenario in which a fraction of tubulin molecules is labeled with a donor fluorophore, a fraction is labeled with an acceptor fluorophore, and the remaining tubulin molecules

are unlabeled (Figure 3.1).

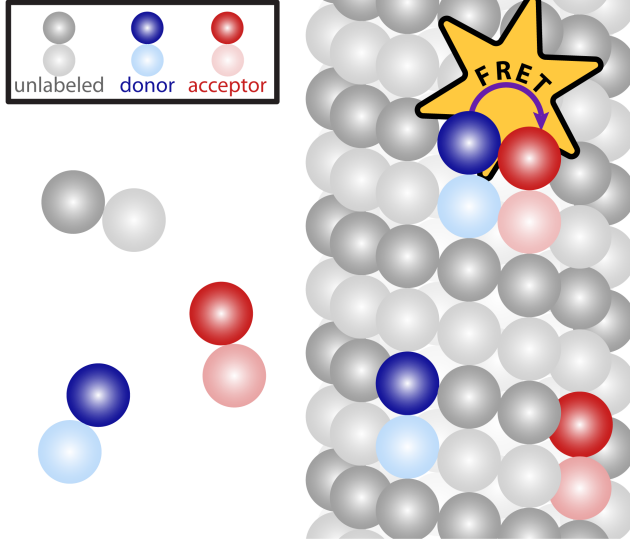


Figure 3.1: Schematic representation of the assumed conditions for FRET. Some tubulin molecules are labeled with a donor fluorophore (blue), some are labeled with an acceptor fluorophore (red), and some are unlabeled (grey). We assume FRET only occurs between a donor-labeled tubulin molecule that is nearby an acceptor-labeled tubulin molecule in a microtubule, while tubulin molecules not incorporated in microtubules are not engaged in FRET.

When this mixture of tubulin is incorporated into a microtubule, we assume that with some probability, P_f , the donor-labeled tubulin neighbors an acceptor-labeled tubulin, allowing for FRET from the donor fluorophore to the acceptor fluorophore. We assume that FRET only occurs between tubulin in a microtubule and use the common two-state model for FRET (Cantor and Schimmel, 1980; Lakowitz, 2006; Mertz, 2010). At a specific location x , we call the fraction of donors engaged in FRET the “FRET fraction”, F , and relate it to the number of donor-labeled tubulin in monomer, N_{mon} , and the number of donor-labeled tubulin in polymer, N_{pol} by:

$$F(x) = \frac{\# \text{ donors that FRET}}{\text{Total donors}} = \frac{P_f N_{pol}(x)}{N_{pol}(x) + N_{mon}} \quad (\text{Eq. 3.2.1})$$

We express $N_{mon}(x)$ as N_{mon} because we assume the monomer concentration does not vary between locations. F is the realization of \tilde{F} , the spectroscopic signal; P_f is the realization of $\lambda_{\tilde{F}}$, an additional parameter that affects the spectroscopic signal; Eq. 3.2.1 is the realization of Eq. 3.1.1. The intensity I is defined as the photon generation rate of donors both engaged and not engaged in FRET per confocal volume:

$$I(x) = \varepsilon [N_{mon} + (1 - P_f)N_{pol}(x) + P_f \alpha N_{pol}(x)] \quad (Eq\ 3.2.2)$$

where ε is the average number of photons detected per donor and α represents the relative brightness of donors engaged in FRET to donors not engaged in FRET. I is the realization of \tilde{I} , the microscopy signal; P_f , ε , and α are realizations of $\lambda_{\tilde{I}}$, the additional global parameters that affect the microscopy signal; Eq. 3.2.2 is the realization of Eq. 3.1.2. By solving for N_{pol} in Eq. 3.2.1 and Eq. 3.2.2, we obtain the relationship between FRET fraction, F , and intensity, I :

$$F(x) = P_f \left(\frac{I(x) - \varepsilon N_{mon}}{I(x) + P_f(\alpha - 1)\varepsilon N_{mon}} \right) \quad (Eq.\ 3.2.3)$$

Eq. 3.2.3 is the realization of Eq. 3.1.3 for this system. A single image provides many locations at which $F(x)$ and $I(x)$ have been measured. If the set of measured $F(x)$ and $I(x)$ agrees with Eq. 3.2.3, it not only validates Eq. 3.2.1 and Eq. 3.2.2, from which Eq. 3.2.3 was derived, but it also allows the parameters εN_{mon} , P_f , and α to be extracted from the fit. If the total concentration of donor in the sample is known (which sets the average value of $N_{pol} + N_{mon}$), then ε can be determined as well.

We combined Eq. 3.2.1 and Eq. 3.2.2 to derive a formula for tubulin in polymer:

$$N_{pol}(x) = \frac{F(x)I(x)}{\varepsilon P_f(1 + (\alpha - 1)F(x))} \quad (Eq. 3.2.4)$$

which is the realization of Eq. 3.1.4. The average tubulin in polymer, N_{pol}^{avg} can be found by averaging the amount of tubulin in polymer over the desired locations,

$$N_{pol}^{avg} = \frac{1}{M} \sum_{x \in image}^M \frac{F(x) I(x)}{\varepsilon P_f(1 + (\alpha - 1)F(x))} \quad (Eq. 3.2.5)$$

where M is the number of locations. In this section, we applied the abstract formalism, presented in the last section, to a FRET-based measurement of polymer amount. In the next section, we construct a molecular FRET probe and test a model that relates fluorescence lifetime to FRET.

MEASURING FRET AND INTENSITY

We use time-domain fluorescence-lifetime imagining (FLIM) with two-photon microscopy to measure $F(x)$ and $I(x)$ (Eq. 3.2.1 and Eq. 3.2.2). To make time-domain fluorescence measurements, a pulse of light is used to raise fluorophores into an excited state. Some of these fluorophores leave the excited state by emitting a photon (Figure 3.2A). These fluorophores stay in the excited state for a characteristic time, called the fluorescence lifetime. By measuring the arrival times of these emitted photons relative to the excitation pulse, we can infer the fluorescence lifetime (Becker, 2010). If the

fluorophore is a donor engaged in FRET, then the fluorescence lifetime of the donor fluorophore will be reduced since FRET provides an additional pathway for the donor to leave the excited state (Figure 3.2A). If there is a subpopulation of donors engaged in FRET, and a subpopulation not engaged in FRET, we expect the measured fluorescent decay to be the sum of each subpopulation's fluorescent decay. If we can measure the fraction of photons that came from a reduced-lifetime emission, then we can infer the fraction of donors engaged in FRET.

While the presence of FRET can lead to a dramatic reduction in the lifetime of a donor fluorophore, other changes in the local environment can also modify the fluorescence lifetime. To analyze the sensitivity of the lifetime of our donor fluorophore, Atto565-labeled tubulin, to changes in its local environment, we used a Bayesian approach to measuring lifetimes (Chapter 2, *Supplemental Materials*). We first investigated the change in lifetime of Atto565-labeled tubulin in purified solutions before and after polymerization. FLIM measurements of 25 μM tubulin (with ~1 in 20 tubulin labeled with Atto565) were fitted with a single exponential model that determined a lifetime of 3.58 ± 0.03 ns for soluble tubulin and 3.45 ± 0.04 ns with tubulin polymerized with 20 μM taxol (Figure 3.2B), where the error is the standard deviation in the lifetimes between three different fields of view. This result demonstrates that incorporation into microtubules does not significantly change the lifetime of Atto565-labeled tubulin in buffer.

Next, we examined if the lifetime of Atto565-labeled tubulin changed after polymerization in *Xenopus* egg extracts. Bayesian analysis of FLIM measurements of 1.2 μM donor-labeled tubulin in extract gave a lifetime of 3.57 ± 0.03 ns. After assembling microtubules with 1 μM taxol, the analysis gave a lifetime of 3.50 ± 0.03 ns. Taken together, these control experiments argue that the lifetime of donor-

labeled tubulin is not significantly altered by local environmental changes that occur during microtubule assembly in extract or buffer.

Next we tested if donor-labeled tubulin could engage in FRET when co-assembled into polymer with Atto647N-labeled tubulin, an acceptor. In the absence of acceptor, we induced 50 μ M tubulin (with ~1 in 4 tubulin labeled with Atto-565) to form microtubules in BRB80 with the addition of 10 μ M taxol. The histogram of photon arrival times was approximately a straight line on a semi-log plot (Figure 3.2C, green curve), suggesting that our donor-labeled tubulin follows a mono-exponential decay in the absence of acceptor. We then created a solution of 50 μ M tubulin with both donor and acceptor (~1 in 2 tubulin being acceptor-labeled and ~1 in 100 donor-labeled) and formed microtubules using taxol. We found the emergence of a short-lifetime decay in the histogram of photon arrival times (Figure 3.2C, purple curve). We attribute the short-lifetime decay to a subpopulation of donor-labeled tubulin engaged in FRET with acceptor-labeled tubulin and the long-lifetime decay component to a subpopulation of donor-labeled tubulin not engaged in FRET. To confirm that the short-lifetime decay was not due to additional non-FRET contributions from the acceptor, such as spectral bleed-through, we repeated the measurement without the addition of taxol. We found that in the absence of microtubules, the decay remained mono exponential (Figure 3.2C, orange curve). Taken together, these experiments argue that the short-lifetime decay seen above is due to FRET between donor and acceptor incorporated into microtubules.

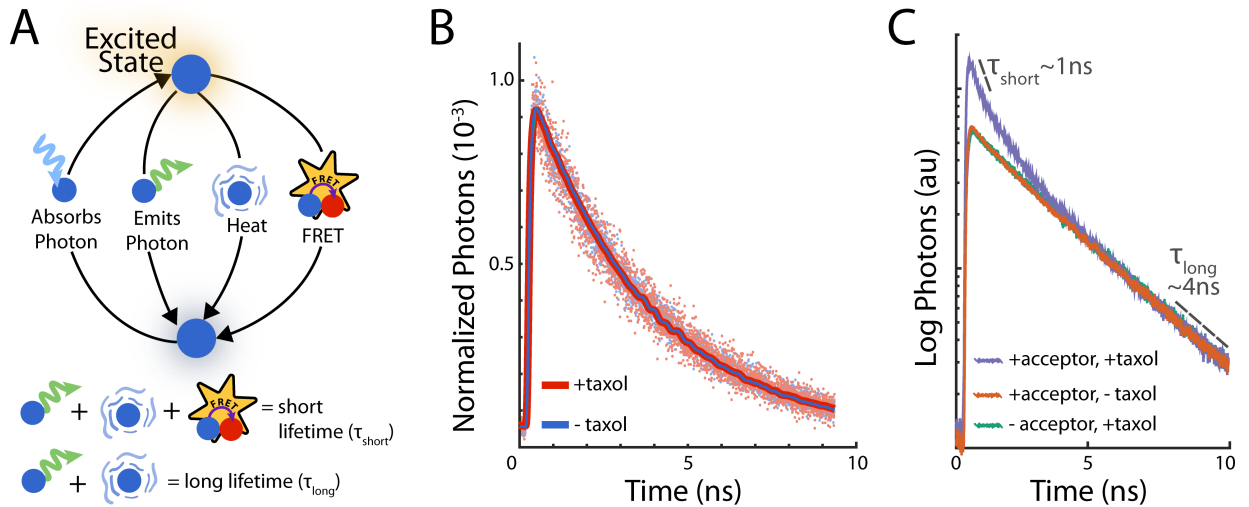


Figure 3.2: Measuring FRET with FLIM. (A) Schematic diagram of excitation and relaxation pathways of the donor (blue) fluorophore. When a donor fluorophore absorbs an incoming photon, the fluorophore is raised into an excited state. The fluorophore relaxes back to the ground state by either emitting a photon or releasing heat. FRET introduces an additional non-radiative pathway for the fluorophore to relax. Thus, the average time the fluorophore spends in an excited state, referred to as the lifetime, is shorter when the fluorophore is engaged in FRET. (B) In purified solutions, in the absence of acceptor, fluorescence-lifetime is not significantly affected by polymerization. Histogram of photon arrival times from Atto-565 conjugated tubulin (donor-labeled tubulin) in taxol-assembled microtubules (red dots) and without taxol (blue dots). Bayesian analysis of these histograms, using a single exponential decay model, estimates the fluorescence-lifetimes (with taxol $3.45 \pm .04\text{ ns}$ and without taxol $3.67 \pm .03\text{ ns}$) and provides the corresponding models (with taxol, red curve and without taxol, blue curve). (C) In purified solutions, taxol-induced microtubules formed in the absence of an acceptor (green) produce a photon arrival-time histogram that is a decaying exponential with a lifetime of $\sim 4\text{ ns}$. FRET happens in the presence of acceptor fluorophore (purple), which induces the addition of a short component with a $\sim 1\text{ ns}$ lifetime.

These results suggest that the photon emission is a sum of two exponentials:

$$y(t) \propto Fe^{\frac{-t}{\tau_{short}}} + (1 - F)e^{\frac{-t}{\tau_{long}}} \quad (\text{Eq. 3.3.1})$$

where $y(t)$ is the number of photons emitted at time t , F is the fraction of donors engaged in FRET, τ_{short} is the lifetime of the donors that are engaged in FRET, and τ_{long} is the lifetime of donors that are not engaged in FRET. We use Eq. 3.3.1 in our Bayesian analysis to estimate $F(x)$ from the histogram

of photon arrival times at each location, x . In order to reduce the number of free parameters, we first obtain the lifetimes in control experiments (*Materials and Methods*). We estimate $I(x)$ as the number of photons collected at location x corrected for stray light and detector dark noise (*Materials and Methods*).

TESTING THE FRET AND INTENSITY RELATIONSHIP IN CELL EXTRACTS

Next we tested our model for the relationship between FRET and intensity for microtubules assembled in cell extracts, which is the basis of our proposed method for measuring microtubule assembly. We first added 1.2 μM donor-labeled tubulin and 1.6 μM acceptor-labeled tubulin to *Xenopus* egg extract and induced microtubule formation with taxol. An intensity image revealed that asters and other large assemblies of microtubules form within minutes of taxol addition (Figure 3.3A), as observed previously (Foster et al., 2015; Verde et al., 1991). In each pixel, we estimated the fraction of donors engaged in FRET to create a FRET fraction map, which displays similar spatial structure to the intensity image (Figure 3.3A). When taxol is not added, and thus no microtubule assembly is induced, relatively little FRET is seen, and intensity images are uniform (Supplemental Figure S3.1).

To test the relationship between FRET fraction and intensity given by Eq. 3.2.3, we made a plot of FRET fraction versus intensity for every pixel (Figure 3.3B, blue dots). While there appears to be a correlation between FRET fraction and intensity, the variance of these points is very large, presumably due to the low number of photons in each pixel. We therefore grouped pixels by intensity and then estimated the FRET fraction and average intensity from donors in each one of these groups (*Materials and Methods*). Plotting the FRET fraction versus intensity of these grouped

pixels revealed a clear trend (Figure 3.3B, black dots), which was well-fit by Eq. 3.2.3 (Figure 3.3B, dashed line), with best-fit values of $P_f = 0.123 \pm 0.006$ and $\varepsilon N_{mon} = 22.0 \pm 2.7$, where α , the relative brightness of donors engaged in FRET to those not engaged in FRET, was previously estimated by the ratio of lifetimes as 0.45. The excellent fit of Eq. 3.2.3 demonstrates the ability of our model to describe the relationship between our microscopy and spectroscopy signal.

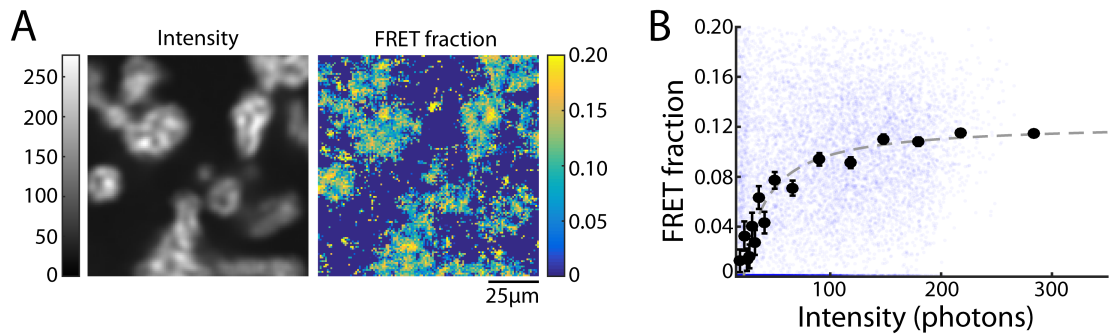


Figure 3.3: Investigating the relationship between FRET fraction and intensity: (A) An intensity image of microtubule structures in extract (left), and corresponding FRET fraction map (right). (B) FRET-fraction vs. intensity from the data in A for individual pixels (small blue dots) and grouped pixels (black dots). Error bars are the standard deviation of the posterior distribution. The grouped pixels are well-fit by Eq. 3.2.3 (dark grey dashed line) with $P_f = 0.123 \pm 0.006$ and $\varepsilon N_{mon} = 22.0 \pm 2.7$, where error is the 95% confidence interval.

The parameters in our model, P_f and εN_{mon} , are not arbitrary fitting parameters, but correspond to physical quantities that can be varied. To further test our model, we varied experimental variables to see if P_f and εN_{mon} changed as expected. The first experimental variable we changed was acceptor concentration. Decreasing acceptor concentration from 1.3 μM to 0.6 μM resulted in similar intensity images and a global reduction in FRET fraction (Figure 3.4A). Grouping pixels as described above, and fitting Eq. 3.2.3 (Figure 3.4B), revealed that εN_{mon} was similar (20.7 ± 3.5 and 16.4 ± 5.6 , respectively) while P_f decreased from 0.107 ± 0.004 to 0.058 ± 0.004 . Thus, as expected, changing acceptor concentration modified the probability of a donor-labeled tubulin in a microtubule engaging

in FRET, P_f without affecting the intensity from soluble monomers, εN_{mon} . To see if this trend continued, we titrated acceptor-labeled tubulin, from 0 μM to 1.6 μM , in increments of 0.32 μM and found that P_f scaled linearly with acceptor concentration (Figure 3.4C) while εN_{mon} remained constant (Figure 3.4D). The observed linear relationship between P_f and acceptor concentration is expected in the low acceptor concentration regime since the probability that at least one neighbor is an acceptor is equal to the fraction of tubulin that is acceptor-labeled. The slope of P_f versus acceptor concentration is proportional to the number of neighbors with which a donor can FRET, which, after taking the endogenous tubulin concentration to be 18 μM (Parsons and Salmon, 1997), gives 1.84 ± 0.16 neighbors (*Materials and Methods*).

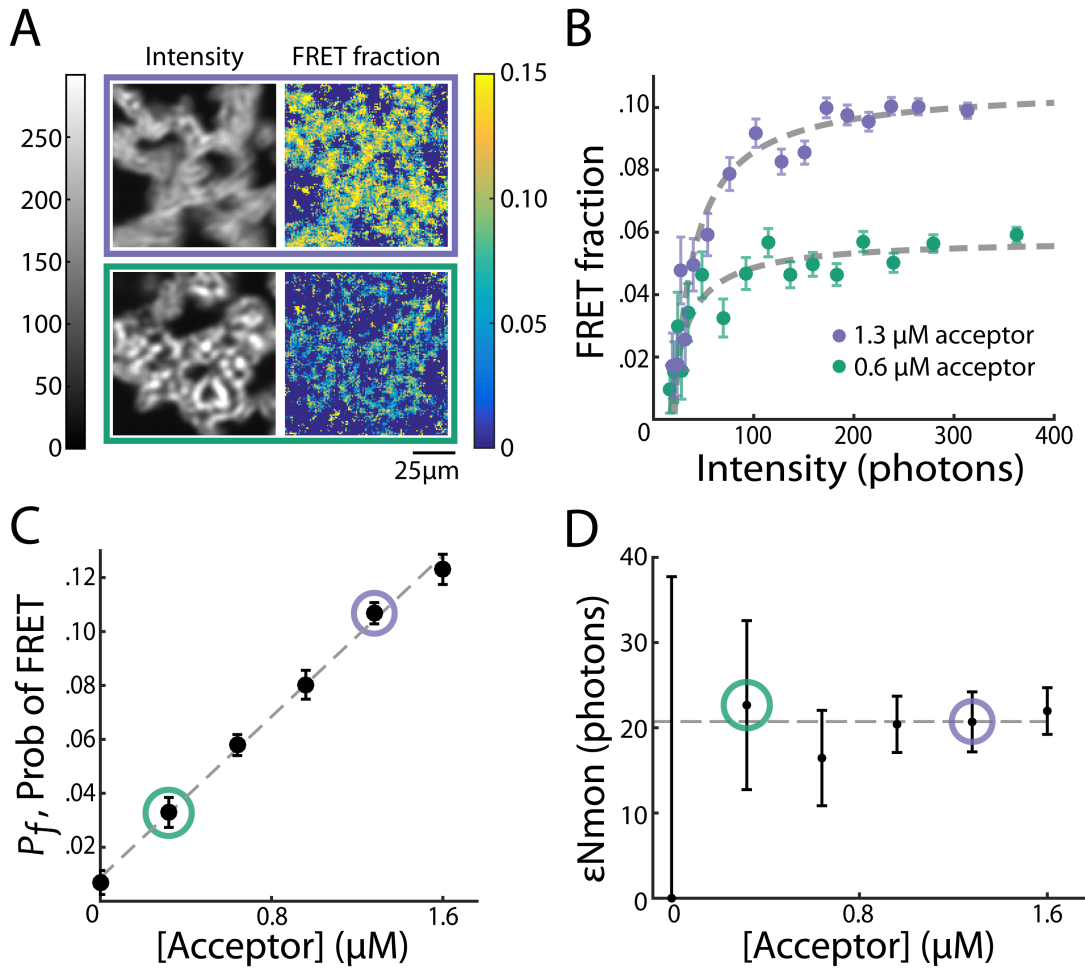


Figure 3.4: Fit parameters change as expected when varying acceptor concentration. (A) Intensity images (left) and FRET fraction maps (right) of taxol induced microtubules in Xenopus egg extracts with high (top) and low (bottom) acceptor concentrations. FRET fraction maps were sensitive to acceptor concentration while the intensity images showed no significant differences. (B) Colored Dots: FRET-fraction and intensity from the data in A for grouped pixels. Error bars are the standard deviation of the posterior distribution. The grouped pixels are well-fit by Eq. 3.2.3 (grey dashed lines) with $P_f = 0.107 \pm 0.004$, $\epsilon N_{mon} = 20.7 \pm 3.5$ for 1.3 μM acceptor and $P_f = 0.058 \pm 0.004$, $\epsilon N_{mon} = 16.4 \pm 5.6$ for 0.6 μM acceptor. Samples with more acceptor have a larger horizontal asymptote, leading to a larger P_f , the probability of FRET. Meanwhile, the x-intercept is unchanged, leading to ϵN_{mon} , the number of photons from donor in monomer, being unchanged. (C) Black dots: P_f , determined from model fitting as shown in B. Colored circles note the P_f values from best-fit of data from samples shown in A and B. Error bars are 95% confidence intervals. P_f increases linearly with acceptor concentration (grey dashed line). (D) Black dots: ϵN_{mon} , determined from model fitting as shown in B. Colored circles note the ϵN_{mon} values from best-fit of data from samples shown in A and B. Error bars are 95% confidence intervals. ϵN_{mon} remains unchanged when acceptor concentration is varied.

Since less photons are collected with shorter acquisition times, we expect εN_{mon} to decrease with decreasing acquisition time. Fixing acceptor concentration (5 μM) and varying acquisition time from 50 seconds to 10 seconds resulted in dimmer images but similar FRET fraction maps (Figure 3.5A). Grouping pixels as described above, and fitting Eq. 3.2.3 (Figure 3.5B), revealed that P_f was similar (0.330 ± 0.012 and 0.313 ± 0.031 , respectively) while εN_{mon} decreased from 76.4 ± 3.5 to 14.8 ± 1.9 . We next systematically varied acquisition time from 5 to 50 seconds in intervals of 5 seconds and found that P_f did not significantly change with acquisition time, as expected since P_f is a property of the sample, not acquisition parameters (Figure 3.5C), while εN_{mon} increased linearly with acquisition time (Figure 3.5D). The linear relationship between εN_{mon} and acquisition time is expected since the number of photons detected depends linearly on acquisition time. Thus, both free parameters, P_f and εN_{mon} , quantitatively varied as expected with changes in experimental conditions, supporting both the model described by Eq. 3.2.1 and 3.2.2 and the accuracy of the experimental system.

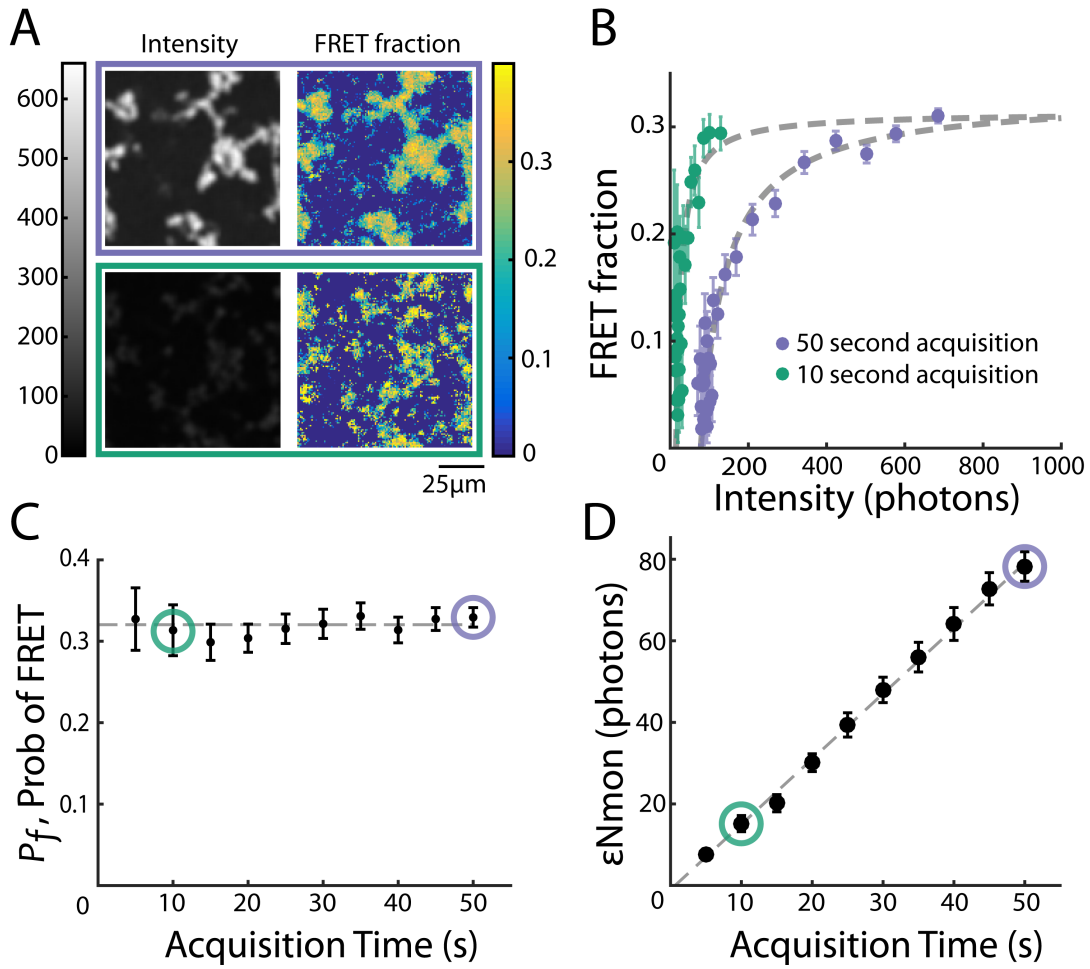


Figure 3.5: Fit parameters change as expected when varying acquisition time. (A) Intensity images and FRET fraction maps of taxol induced microtubules in *Xenopus* egg extracts acquired with a long (purple) and a short (green) acquisition time. Shorter acquisition times resulted in dimmer images but similar FRET fraction maps. (B) Colored Dots: FRET-fraction and intensity from the data in A for grouped pixels. Error bars are the standard deviation of the posterior distribution. The grouped pixels are well-fit by Eq. 3.2.3 (grey dashed line) with $P_f = 0.330 \pm 0.012$, $\epsilon N_{mon} = 76.4 \pm 3.5$ for 50 second acquisition and $P_f = 0.313 \pm 0.031$, $\epsilon N_{mon} = 14.8 \pm 1.9$ for 10 second acquisition. The x-intercept increases with acquisition time, leading to a larger ϵN_{mon} . Meanwhile, the horizontal asymptote, which determines P_f , remains unchanged. C) Black dots: P_f , determined from model fitting as shown in B. Colored circles note the P_f values from best-fit of data from samples shown in A and B. Error bars are 95% confidence intervals. P_f remains unchanged when acquisition time is varied (grey dashed line). D) Black dots: ϵN_{mon} , determined from model fitting as shown in B. Colored circles note the ϵN_{mon} values from best-fit of data from samples shown in A and B. Error bars are 95% confidence intervals. ϵN_{mon} increases linearly with acquisition time (grey dashed line).

MEASURING POLYMER CONCENTRATION

After validating the FRET and intensity measurements of microtubules, we next sought to test if this assay could accurately determine polymer concentration. To do this, we created three dilution series of taxol-stabilized microtubules with 8.3% donor-labeled tubulin, 16.7% acceptor-labeled tubulin, and 75% unlabeled tubulin in BRB80. To find ε , we first created a sample containing 50 μM tubulin and measured P_f and εN_{mon} through fitting Eq. 3.2.3 to the FRET fraction and the intensity of grouped pixels (as described above). Using these values, we then calculated εN_{pol} with Eq. 3.2.5. We divided the sum of εN_{pol} and εN_{mon} by the known tubulin concentration to obtain ε in units of photons per micromolar of tubulin.

The amount of polymer was measured in six fields of view for each sample in the microtubule dilution series by finding P_f and εN_{mon} through fitting Eq. 3.2.3 to the FRET fraction and the intensity of grouped pixels (as described above). We then calculated the polymer concentration in each field of view with Eq. 3.2.5. The polymer concentration, when averaged over fields of view, was similar to the tubulin concentration for the entire dilution series (Figure 3.6, green dots). This was expected due to the high molarity of taxol, which causes the majority of tubulin to be in polymer. To compare our methodology to an established technique, we then recreated in triplicate the microtubule dilution series without labeled tubulin. The dilution series was centrifuged, solubilized, and the pellet was depolymerized in ice-cold BRB80. We then measured the concentration of tubulin by 280 nm absorption three times for each sample (Figure 3.6, blue dots). We found that our measurement was in good agreement with the polymer concentration measured using ultracentrifugation. Unlike ultracentrifugation, which provides a measurement of polymer averaged across a sample, our measurements are spatially resolved. To illustrate this advantage, we calculated the polymer concentration at each location within a field of view using Eq. 3.2.4 (Figure 3.6, inset). These results,

in conjunction with our previous findings, illustrate how our methodology can be used to construct time-resolvable, non-destructive assays that faithfully measure polymer concentration.

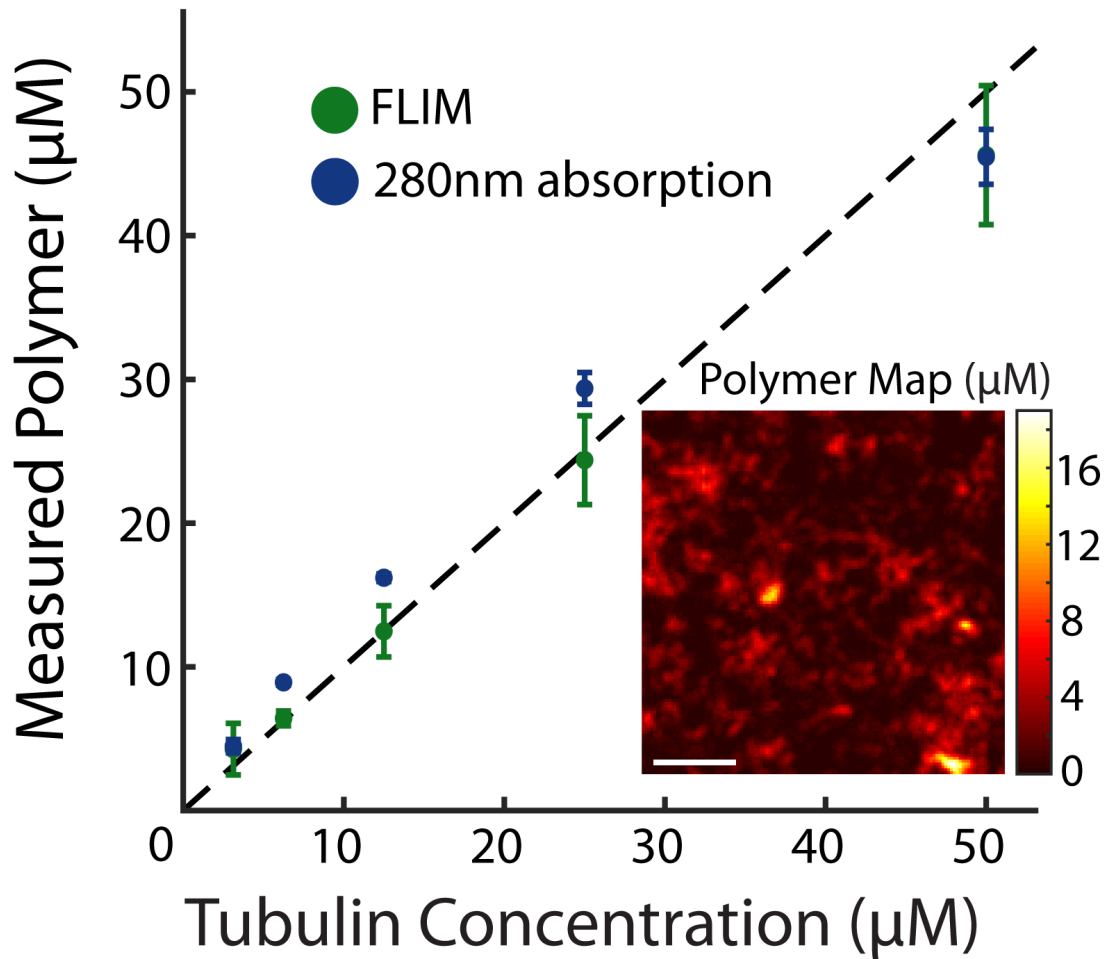


Figure 3.6: Microtubule dilution series to test measurements of polymer concentration. Polymer measurements by FRET-intensity (green dots) and centrifugation followed by absorption at 280 nm (blue dots) correspond to the expected polymer amount (black dashed line). Error bars are standard error of the mean. (Inset) Map of the concentration of tubulin subunits in polymer. Scale bar, 25 μm .

TESTING THE METHODOLOGY IN CELLS

We next tested how the methodology could be applied to another system: FRET measurements of spindles in cells. To obtain cells with fluorescently labeled tubulin, we created a stable cell line of U2OS cells expressing SNAP-tag- α -tubulin and incubated these cells with JF549-cpSNAP-tag, our donor fluorophore, and JF646-SNAP-tag, our acceptor fluorophore (*Materials and Methods*). We performed FLIM measurements on mitotic cells, revealing spindles when viewed with two-photon intensity imaging (Figure 3.7). We then segmented the image to include only the spindle region and found the lifetimes of donors engaged in FRET and not engaged in FRET (*Materials and Methods*). We grouped pixels as described above and saw a clear relationship between FRET fraction and intensity (Figure 3.7, purple dots) which was well fit by Eq. 3.2.3 (Figure 7B, purple dashed line), with best-fit values of $P_f = 0.091 \pm 0.008$ and $\varepsilon N_{mon} = 19.9 \pm 4.6$, where α , the relative brightness of donors engaged in FRET to those not engaged in FRET, was previously estimated by the ratio of lifetimes. The fit of Eq. 3.2.3 demonstrates the ability of the model to describe the relationship between FRET and intensity within subcellular structures in these cells. In the absence of acceptor, the measured FRET fraction was drastically reduced and this relationship disappeared (Figure 3.7B, green dots), arguing that the measured FRET was due to FRET from donor- to acceptor-labeled tubulin. We next sought to use this method to measure the concentration of microtubules in spindles by applying equation Eq. 3.2.5. This procedure requires measuring ε . To find ε in units of photons per micromolar tubulin, we use the fact that tubulin must be in either monomer or polymer, thus:

$$N_{pol} + N_{mon} = N_{Total}$$

where N_{Total} is the total number density, or total concentration of tubulin. Combining this equation with Eq. 3.2.1 and Eq. 3.2.2 gives

$$\varepsilon = \frac{I}{N_{Total} (1 + (\alpha - 1) F)}$$

This equation holds true for any volume. N_{total} averaged over the cell has been reported to be $20 \mu\text{M}$ (Hiller and Weber, 1978); combining this value with FRET fraction, F , and intensity, I , measurements averaged over the cell, allowed us to calculate ε in an individual cell. We then segmented the spindle from the image and found P_f through fitting Eq. 3.2.3 to FRET fraction and intensity of grouped pixels. We use these values in Eq. 3.2.5 to estimate the microtubule concentration to be $39 \pm 3 \mu\text{M}$ in the spindle, where the error is the standard deviation between cells ($n=6$). These results show the applicability of the methodology in both cell extracts and cells.

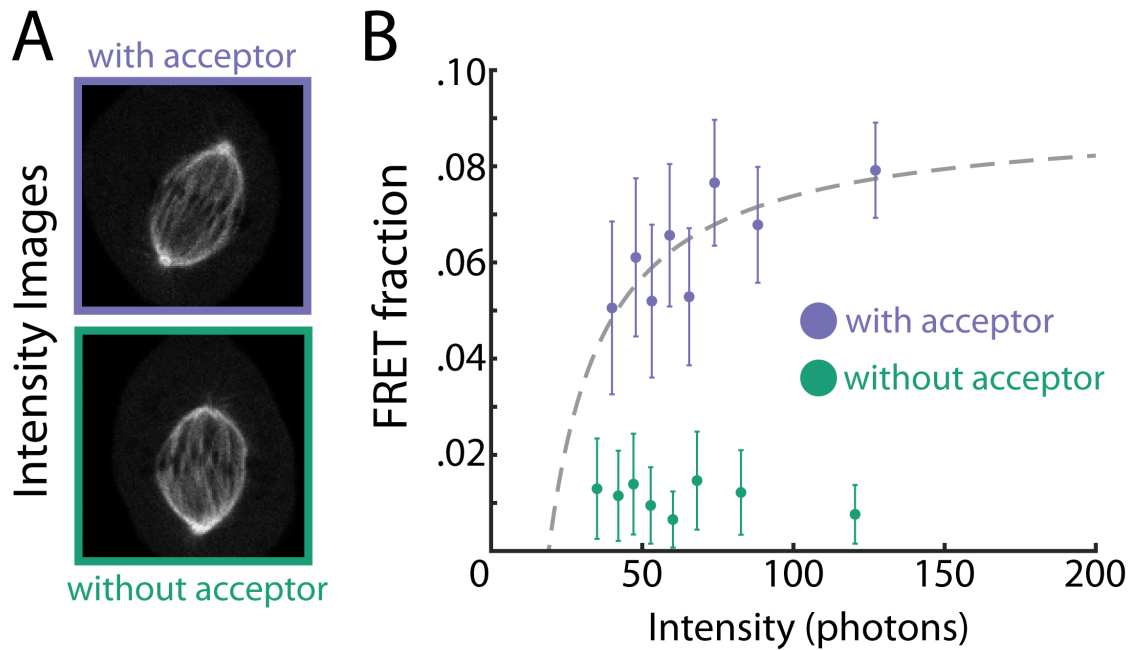


Figure 3.7: Investigating the relationship between FRET fraction and intensity in U2OS cells: (A) An intensity image of a mitotic spindle from a cell with both donor- and acceptor-labeled tubulin (top) and from a cell with only donor-labeled tubulin (bottom). (B) Colored Dots: FRET-fraction and intensity from the data in A for grouped pixels. Error bars are the standard deviation of the posterior distribution. The grouped pixels from the sample with both donor and acceptor is well-fit by Eq. 3.2.3 (grey dashed lines) with $P_f = 0.091 \pm 0.008$ and $\varepsilon N_{mon} = 19.9 \pm 4.6$, where error is the 68% confidence interval.

*D*ISCUSSION

Time-resolvable quantitative measurements of polymer concentration are very useful for studying protein polymerization pathways. It is difficult to construct such quantitative readouts of polymer in cells and cell extracts. While fluorescence microscopy and spectroscopic methods are often used to measure polymer amount, fluorescence microscopy can be insensitive to measuring polymer amount for early time points after nucleation when polymers are small, whereas spectroscopic measurements can be hard to interpret and are subject to many artifacts. We developed a methodology to utilize microscopy and spectroscopy measurements simultaneously to overcome the limitations of both approaches in cells and cell extracts.

First, we constructed a model that describes how the intensity and FRET fraction depend on the partitioning of subunits into monomer and polymer. The model predicts that FRET and intensity are related to each other due to the presence of polymer (Eq. 3.2.3). We then used a combination of two-photon microscopy with FLIM to simultaneously measure intensity, our microscopy signal, and FRET, our spectroscopy signal, at each pixel in an image. We then grouped these pixels to test the relation between FRET fraction and intensity and found that Eq. 3.2.3 described the data remarkably well. This supports the validity of each of the measurements. We also observed that the best-fit values of the two free parameters quantitatively changed as expected with changes in the experimental variables. We then showed that our combined microscopy-spectroscopy technique

recapitulated the average measurements of ultracentrifugation while providing spatially resolved measurements. We applied our methodology to validate a new polymer measurement system in cells. Finally, we applied this measurement system to estimate the microtubule concentration within a subcellular structure: the spindle.

We used approximations to make a tractable model, including a two-state model for FRET, that all donors in polymer are equally likely to FRET, and that the fraction of donors engaged in FRET is linearly related to the amount of polymer. The net effect of our approximations is presumably very small, as suggested by the quantitative agreement between the model and the data under many different conditions. Using simplifying assumptions reduces the number of free parameters, allowing for testing of the model with data—without over-fitting.

In our model, the definition of “the number of monomers”, N_{mon} , uses the necessary condition for the monomer; monomeric tubulin does not FRET. That is, the monomeric tubulin is assigned to N_{mon} , but N_{mon} doesn’t necessarily imply monomeric tubulin. For example, we observed in our FRET-intensity plots that low-intensity pixel groups have no measurable FRET but have considerable intensity. These pixel groups presumably represent freely diffusing tubulin. In our model, these pixel groups do not contain tubulin species corresponding to N_{pol} , which generates FRET signal, but only N_{mon} , which do not FRET. N_{mon} can be interpreted not only as single alpha-beta tubulin units, commonly referred to as monomeric tubulin, but also as oligomers that cannot generate FRET. Therefore, there may be multiple interpretations of tubulin species that exhibit no FRET. The first possible interpretation is that there are freely diffusing oligomers, but these oligomers cannot generate FRET. One way this could happen is that monomeric tubulins are aggregated by the protein stathmin, which links two monomeric tubulins (Belmont and Mitchison,

1996; Curmi et al., 1997; Gigant et al., 2000), but these aggregated tubulins are too far apart from each other to FRET. Another possibility is that FRET happens in tubulin that is in a certain conformation present in microtubules, while tubulins in oligomers are in a different geometry that generates small or no FRET. The second possible interpretation on the low-intensity, no-FRET pixels is that there are little or no freely diffusing oligomers, though oligomers generate FRET; that is, N_{mon} consists only of monomeric tubulins. One way this could happen is that oligomers are highly unstable during microtubule formation, which makes its population very minor compared to monomers and large microtubules.

A unique advantage of this method is the cross-validation of the spectroscopic measurement and the microscopy measurement. In cells, it is challenging to precisely control the acceptor concentration and changes in acceptor concentration can vary how FRET relates to polymer. Simultaneous measurements of FRET and intensity allow this difficulty to be overcome by cross-validation in each cell. Another advantage of combining microscopy and spectroscopy measurements is that the resulting polymer measurement has a broader range of sensitivity. The microscopy measurement is sensitive to the change in polymer amount in the high polymer regime. This is because intensity increases linearly with the amount of polymer in the high polymer limit. However, due to the presence of soluble subunits, the fractional change in intensity is small in the low polymer regime. On the other hand, polymer measurements by FRET are sensitive to the change in polymer amount in the low polymer regime. FRET fraction linearly increases with the polymer amount in the low polymer limit. However, FRET only marginally changes in the high polymer regime because in this limit, large changes in the amount of polymer correspond to small changes in the fraction of subunits in polymer (which, by construction, cannot exceed 1). Therefore, combining two measurements enables us to measure changes in polymer amount both in the high and low polymer regimes.

In summary, we combined microscopy and spectroscopy measurements to build a novel system for collecting microtubule polymerization curves in cell extracts. This methodology can be applied to any protein complex, and any set of spectroscopy and microscopy measurements. Here we used two-photon microscopy, but other microscopy methods, such as TIRF or super-resolution microscopy, can be used. While FRET was used in this study, other spectroscopy signals, such as steady-state anisotropy for measuring rotational diffusion times or homoFRET, can be used. Our method is particularly well-suited for experiments requiring high-temporal resolution, as in polymerization curve measurements, high-spatial resolution, as in subcellular measurements, or non-destructive measurements, for example if a single cell time-course is required. We hope this framework will allow researchers to develop new quantitative polymer assays to study other polymer assembly pathways.

METHODS

SAMPLE PREPARATION

Samples were observed in a conventional flow cell. Bovine tubulin was purified and labeled with fluorophores as previously described (Mitchison and Kirschner 1984; Hyman et al., 1991, Mitchison lab, 2012). CSF-arrested egg extracts were prepared from *Xenopus laevis* oocytes as described previously (Hannak and Heald, 2006). Tubulin was polymerized in egg extracts by adding donor labeled tubulin to 1.2 μ M and taxol (in DMSO) to 5 μ M at room temperature unless otherwise noted.

To make microtubule dilution series, we mixed unlabeled and labeled tubulin together in BRB80 with 1 mM DTT and 1 mM GTP. This was incubated on ice for 5 minutes before 1/10 volume of 1 μ M taxol per μ M tubulin was slowly added. This mixture was then incubated at 37°C for 10 minutes before 1/10 volume of 10 μ M taxol per μ M tubulin was slowly added. This mixture was then incubated at 37°C for 10 minutes. To create the microtubule dilution series, the polymer solution was diluted by factors of two into polymerization buffer, which is composed of 50 μ M taxol, 10% DMSO (v/v), 1mM DTT, 1mM GTP, and BRB80.

U2OS cell lines were maintained in Dulbecco's modified Eagle's medium (DMEM, Gibco) supplemented with 10% Fetal Bovine Serum (FBS, Gibco), and 50 IU/mL penicillin and 50 μ g/mL streptomycin (Gibco) at 37°C in a humidified atmosphere with 5% CO₂. A stable U2OS cell line expressing SNAP-tag- α -tubulin was generated through a retroviral transfection with 200 μ g/mL hygromycin (Gibco) selection. For live-cell imaging, cells were grown on a 25-mm diameter, #1.5-thickness, circular cover glass coated with poly-D-lysine (GG-25-1.5-pdl, neuVitro) to 80~90% confluence. To associate SNAP-tag- α -tubulin with fluorescent SNAP-tag ligands, the cells were incubated for 30 minutes with 150 nM JF549-cpSNAP-tag for negative control experiments, or with both 150 nM JF549-cpSNAP-tag and 1350 nM JF646-SNAP-tag ligands for FRET experiments, followed by washing three times with DMEM (Grimm et al., 2015). Then the cells were incubated in imaging media, which is FluoroBrite™ DMEM (Gibco) supplemented with 4mM L-glutamine (Gibco) and 10mM HEPES, for ~15-30 minutes before imaging. The cover glass was mounted on a custom-built temperature controlled microscope chamber at 37°C, and covered with 1.5 ml of imaging media and 2 ml of white mineral oil (VWR). An objective heater (Bioptronic) was used to maintain the objective at 37°C.

MICROSCOPY

Our microscope system was constructed around an inverted microscope (Eclipse Ti, Nikon, Tokyo, Japan), with a Ti:sapphire pulsed laser (Mai-Tai, Spectra-Physics, Mountain View, CA) for two-photon excitation (1000 nm wavelength, 80 MHz repetition rate, ~70 fs pulse width), a commercial scanning system (DCS-120, Becker & Hickl, Berlin, Germany), and hybrid detectors (HPM-100-40, Becker & Hickl). The excitation laser was collimated by a telescope assembly to fully utilize the numerical aperture of a water-immersion objective (CFI Apo 40 WI, NA 1.25, Nikon) and avoid power loss at the XY galvanometric mirror scanner. The fluorescence from samples was imaged with a non-descanned detection scheme with a dichroic mirror (705 LP, Semrock) that was used to allow the excitation laser beam to excite the sample while allowing fluorescent light to pass into the detector path. A short-pass filter was used to further block the excitation laser beam (720 SP, Semrock) followed by an emission filter appropriate for Atto565-labeled tubulin (590/30nm BP, Semrock).

PHOTON ARRIVAL-TIME HISTOGRAMS

We use a Becker and Hickl Simple-Tau 150 FLIM system to record photon arrival-time histograms. All arrival times are measured relative to the excitation of a photodiode that is triggered by the excitation laser (Becker, 2010). The TAC range was set to 7×10^{-8} , with a gain of 5, corresponding to a 14 ns maximum arrival time. The TCSPC system can lose fidelity for photons that arrive just before or after the excitation of the photodiode (Becker, 2010), and thus we set the lower and upper limits to 10.59 and 77.25, respectively, resulting in a ~10 ns recording interval. The instrument response function was measured using fixed-point illumination of second harmonic generation of a urea crystal. For most measurements, the intensity of the illumination beam was set such that there were

approximately 100,000 photons per second recorded. Data was acquired as a 128x128 pixel image, where a corresponding photon arrival-time histogram was recorded for each pixel.

POLYMER MEASUREMENTS BY ABSORPTION

Tubulin concentration was determined using a NanoDrop spectrophotometer with an extinction coefficient of $1.15 \text{ (mg/ml)}^{-1}\text{cm}^{-1}$ (Widlund et. al., 2012).

DATA ANALYSIS

Estimating the FRET fraction and Intensity from Photon Arrival Histograms: We use a Bayesian model to build posterior distributions from photon arrival-time histograms (*Supplemental Materials*). The posterior was evaluated at uniformly spaced grid points in parameter space. Point estimates of the FRET fraction were found by taking the maximum of the posterior distribution of the FRET fraction. To reduce the number of free parameters when analyzing photon arrival histograms to find the FRET fraction, we first found the two lifetimes of the donor fluorophore, and then fixed those lifetimes in our Bayesian analysis. This reduced the number of free parameters from four to two. Intensity is defined as the number of photons from donors per pixel per acquisition. The number of photons from donors is found by taking the product of the number of photons and the expected value of the fraction of photons from donors.

We used the following procedure to find lifetimes in each day's freshly prepared extract, U2OS cells, and for our experiments in buffer. To find τ_{long} , the lifetime from donors not engaged in FRET, we measured a sample that had no acceptor-labeled tubulin (i.e., no FRET), and then used a single-exponential decay model in our Bayesian analysis to find the maximum a posteriori estimate lifetime.

Then, we measured a sample that had both donor and acceptor in microtubules, fixing the newly found τ_{long} and built a posterior distribution on the fraction of photons from donors engaged in FRET, not engaged in FRET, and the lifetime of donors engaged in FRET (τ_{short}). The maximum a posteriori estimate was used as the point estimate for the value of τ_{short} . These estimates of lifetimes were then used in the analysis for all measurements performed on that day's extract. For cell data, only FLIM decays from the spindle region were used to determine lifetimes. To analyze FLIM decay curves from only the spindle region, we applied the Gaussian blur function from MATLAB followed by thresholding to the intensity image. The resulting image was used as a mask for the original FLIM data.

For FRET fraction measurements in extract, we remove the first 0.6 ns from the photon arrival-time histograms—as measured from the maximum of the photon arrival-time histogram—to filter out very short-lifetime photons that come from endogenous fluorescence. Since our model does not consider the time decay of extract fluorescence, removing early time bins makes the data more consistent with our model, which assumes photons only come from donors and stray light and detector dark noise (*Supplemental Materials*). For FRET fraction measurements in buffer, we remove the first 0.2 ns.

Fit Parameters and Error Bars: For figures 3.3B, 3.4B, 3.5B, and 3.7B error bars are 68.2% credible intervals. To obtain best-fit parameters and confidence intervals, we used the weighted fit function from MATLAB to fit Eq. 2.3, where the weights are the inverse of the standard deviation of the posterior distribution of the FRET fraction. Reported errors in the best-fit values of the parameters are the 95% confidence intervals, except for figure 3.7B which uses a 68% confidence interval. For figures 3.4C, 3.4D, 3.5C, and 3.5D, we used the weighted fit function from MATLAB, where the

weights are the square of the inverse of the standard deviation, where standard deviation was estimated as half of the 68.2% confidence interval. The error bars in Figure 3.6 are estimated as the standard error of the mean from 3 different microtubule dilution series, where polymer amount was measured 3 times for each sample using 280 nm absorption, and in six fields of view for each sample in FRET-intensity measurements.

Constructing Intensity Images and FRET fraction and Polymer Maps: For figures 3.3A and 3.4A, the photon arrival-time histograms of ten consecutive twenty-second acquisitions were summed at each pixel. To boxcar average each pixel, we summed the photon arrival-time histogram at each pixel with the closest 24 pixels. We then applied our Bayesian analysis on the resulting photon arrival-time histogram to find the FRET fraction at each boxcar-averaged pixel and the fraction of total photons that came from donors. The intensity map was created by dividing the total number of photons in the boxcar-averaged pixel by the number of pixels used in the boxcar average (25) and the number of acquisitions (10 for figure 3.3A and 3.4A, one for figure 3.5A). For the polymer map presented in the inset of figure 3.6, we boxcar averaged each pixel with the closest 8 pixels.

Grouping Pixels: Pixels were sorted by photon counts into pixel groups, where each pixel group is composed of the same number of pixels. The photon arrival-time histogram for the pixel group was constructed by adding the histograms of each pixel in the group. To avoid bias due to low photon counts, no pixel group has less than 10,000 photons.

4

MICROTUBULES ACTIVATE MICROTUBULE
NUCLEATORS

Mitotic spindle assembly is tightly regulated by the nucleation of microtubules. It is thought that nearly all microtubules are nucleated by accessory proteins called nucleators. The γ -tubulin ring complexes (γ TuRCs) is thought to be the central microtubule nucleator (Kollman et al., 2011). These complexes function as a template for the assembly of the 13 protofilaments that make up a microtubule. γ TuRC caps the microtubule minus end, whereas tubulin dimers are added to the microtubule plus end. Once microtubules have nucleated, they will grow steadily before depolymerizing rapidly, until completely depolymerized. The average lifetime of a microtubule before depolymerizing was found to be \sim 20 seconds (Needleman et al., 2010).

Many microtubules are nucleated from centrosomes in most metazoan cells. Over a hundred years ago, centrosomes were identified at the center of the spindle poles and were originally thought to be the central player in spindle assembly. However, meiotic cells lack centrosomes yet still form spindles, and thus microtubules, near chromosomes. In addition, most metazoan cells can still form a functioning spindle when centrosomes are removed (Khodjakov et al., 2000; Megraw et al., 2001). Since microtubules only form near chromosomes, this lead researchers to investigate chromosomal nucleation pathways. In the 1990s it was established that the RAN pathway, the same pathway used in interphase for nuclear import, was used to promote nucleation near chromosomes. Recently, studies suggest that nucleators regulated by the chromosomal pathway may be regulated by microtubules themselves (Petry et al., 2013; Kamasaki et al., 2013; Hsia et al., 2014; Ho et al., 2011; Wieczorek et al., 2015; Roll-Mecak et al., 2006). This evidence primarily stems from observing that nucleators, and the microtubules that grow from them, are localized to other microtubules. This phenomenon is termed “branching” (Petry et al., 2013). However, it remains unclear whether nucleators are activated by the other microtubules, or if they are simply localized to microtubules. In

this chapter, we will investigate two extreme models. In the *bound nucleation* model, nucleators are only active when bound to microtubules. In the *all nucleation* model, nucleators nucleate at a rate which is not dependent on whether they are bound to another microtubule (Figure 4.1).

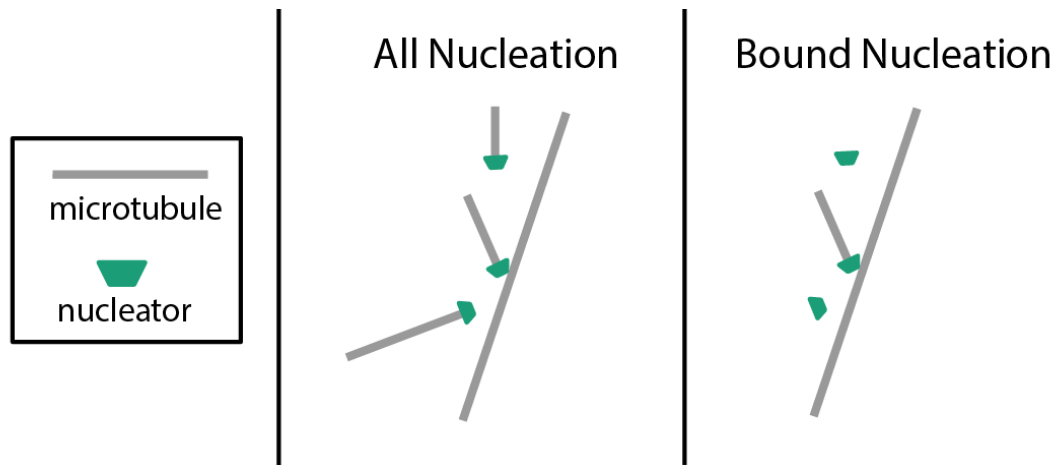


Figure 4.1: Schematic representation of two extreme models of nucleation. In the *all nucleation* model, nucleator activity is not affected by other microtubules. In the *bound nucleation* model, nucleators can only nucleate when bound to microtubules.

It is challenging to decouple nucleator localization from nucleator activation in the spindle because the density of microtubules is too high to resolve individual filaments, let alone individual nucleation events. Furthermore, microtubules may bind to other microtubules after nucleation has occurred. Therefore, we will look at the boundary of the spindle, where nucleators can diffuse away from the spindle, to measure their activity (Figure 4.2). Order-of-magnitude calculations suggest that nucleators would continue to nucleate for at least 10 μm outside of the spindle before being deactivated (Supplement).

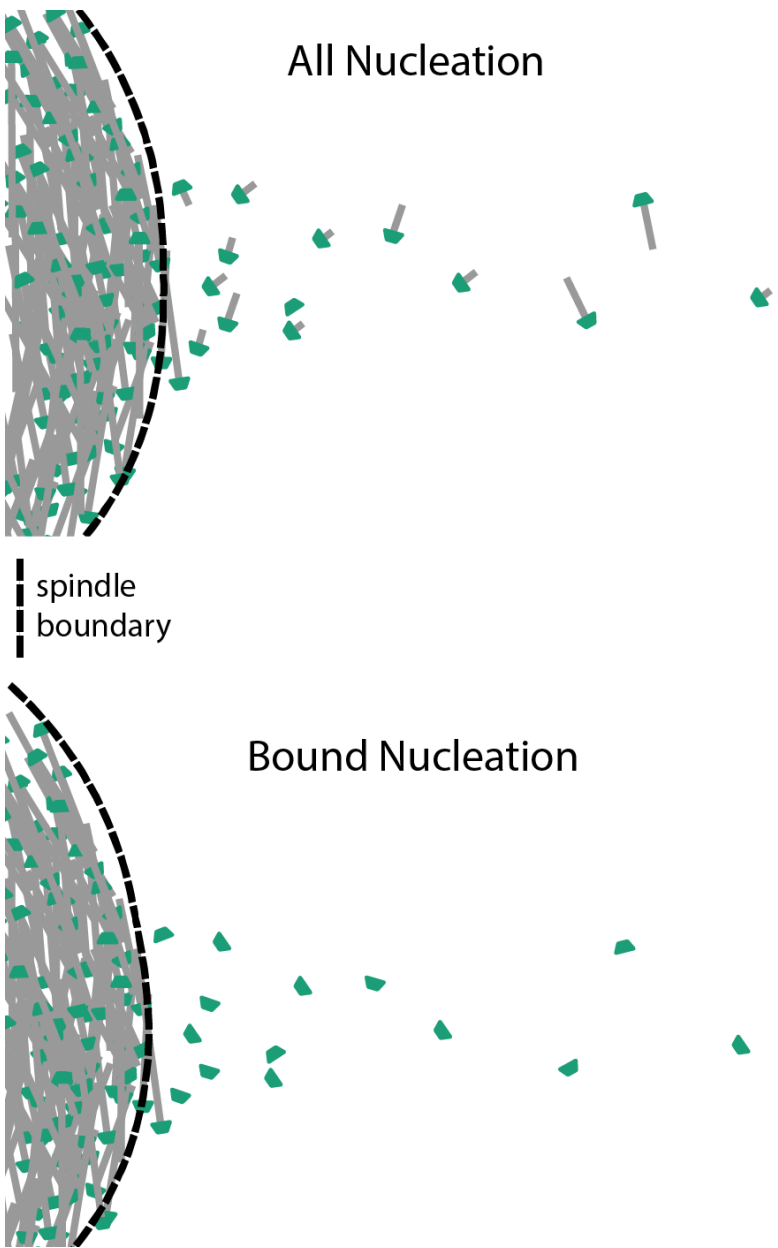


Figure 4.2: Schematic representation of nucleators diffusing away from the spindle boundary. (Top) In the *all nucleation* model, nucleators continue to create polymer as they diffuse away from the spindle. This predicts a gradient in polymer concentration. (Bottom) In the *bound nucleation* model, there is no gradient in the polymer concentration away from the spindle boundary.

In order to measure this possible gradient, we utilized the polymer measuring system described in Chapter 3. In short, we add donor- and acceptor-labeled tubulin to *Xenopus laevis* egg extract. When

the donor and acceptor are localized together, which can happen in microtubules, FRET can occur. When tubulin is soluble, FRET does not occur. FLIM measurements reveal the fraction of tubulin engaged in FRET (Figure 4.3). Measurements of fluorescence intensity is proportional to the total amount of tubulin at each location. Thus, by using FLIM measurements of FRET, in conjunction with intensity measurements, we can measure polymer concentrations.

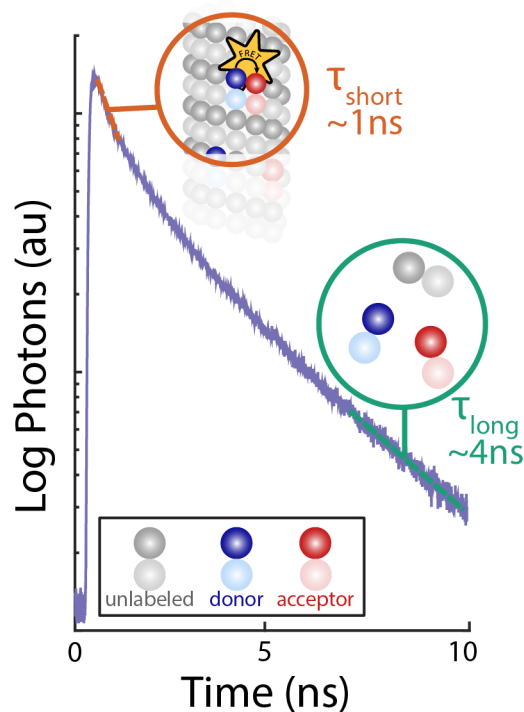


Figure 4.3: FLIM measurements of FRET reveal polymer fraction. Tubulin in microtubules can FRET, which produce photons with a short lifetime. Soluble tubulin cannot FRET, and produce photons with a long lifetime. FLIM histograms can therefore be used to measure the fraction of tubulin in polymer.

Since the spindle is an asymmetric structure, it seemed plausible that the polymer gradient depended on angle. To test this, we added donor- and acceptor-labeled tubulin to extract and formed spindles

(*Methods*). We imaged spindles for multiple 10-second acquisitions and registered the acquisitions to form one image (*Methods*). We then found the spindle boundary by thresholding the intensity image, and segmented the image into pixels that were equidistant from the spindle boundary. Pixels within the spindle boundary were considered to have a negative distance, while pixels outside the boundary were considered to have a positive distance. These pixels were then split up by angle into 4 separate quadrants; 2 quadrants corresponding to the poles of the spindles, and 2 corresponding to the mid-body (Figure 4.4 left). The photons corresponding to the pixels at each distance (in 1.5 μm intervals) were then pooled and analyzed to find the FRET fraction and intensity (Figure 4.4 middle). These intensity and FRET measurements were analyzed in each group and used to find the polymer concentration as a function of distance from the spindle edge. (Figure 4.4 right). Each quadrant exhibited similar spatial dependence on FRET, intensity, and polymer concentrations, indicating a lack of asymmetry. Furthermore, no apparent gradient in polymer concentration could be seen.

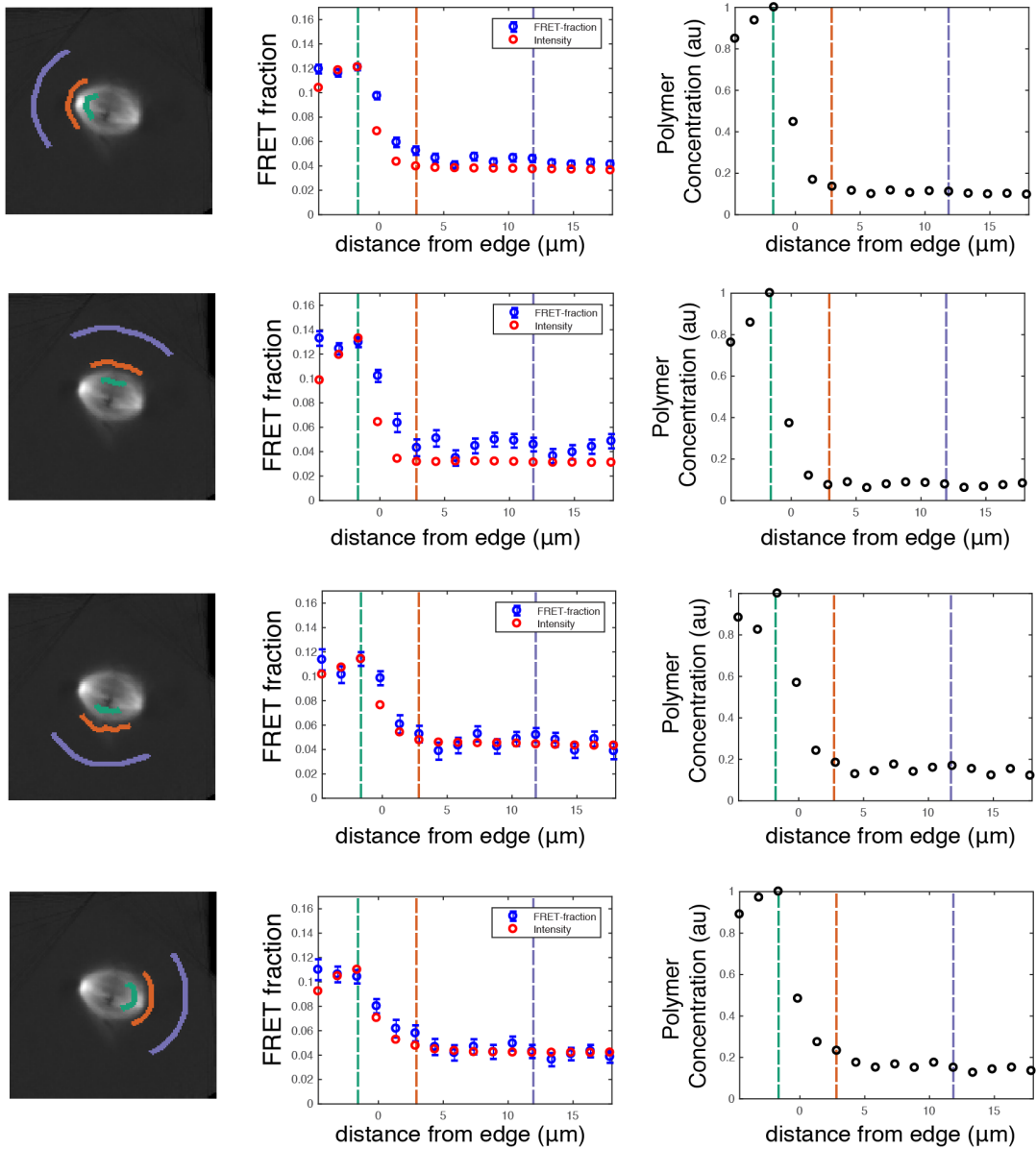


Figure 4.4: Polymer concentration versus distance shows no significant angle dependence. (Left) Intensity images of spindles. Pixels are segmented into groups by their minimum distance from the spindle boundary in an angle dependent fashion. Grouping of pixels at a negative distance (green), small positive distance (orange), and large positive distance. (Middle) FRET fraction (blue) and intensity are measured in each pixel group to give a FRET versus distance and intensity versus distance graph. The grouping shown in (left) are denoted by dashed lines in the graph. (Right) Using the FRET and intensity data in (middle), polymer concentration versus distance is calculated. The grouping shown in (left) are denoted by dashed lines in the graph.

Due to this angular symmetry, we next decided to segment pixels based solely on their distance from the spindle boundary. As the error in the FRET fraction measurement is determined by the number of photons, the spatial resolution is limited by the minimum amount of pixels we can have in a group and still maintain reasonable error bars on the FRET fraction. Averaging over all angles allowed us to measure polymer in 0.5 μm intervals. We then analyzed FRET, intensity, and polymer concentrations as previously described for 12 spindles (Figure 4.5). All spindles, independent of their size, mid-body microtubule density, and the qualitative attribute of “quality”, exhibit the same lack of polymer gradient. This argues that this lack of gradient is robust to microtubule interactions and microtubule density, which suggests that this aspect of microtubule nucleation is fundamental and insensitive to many environmental variables.

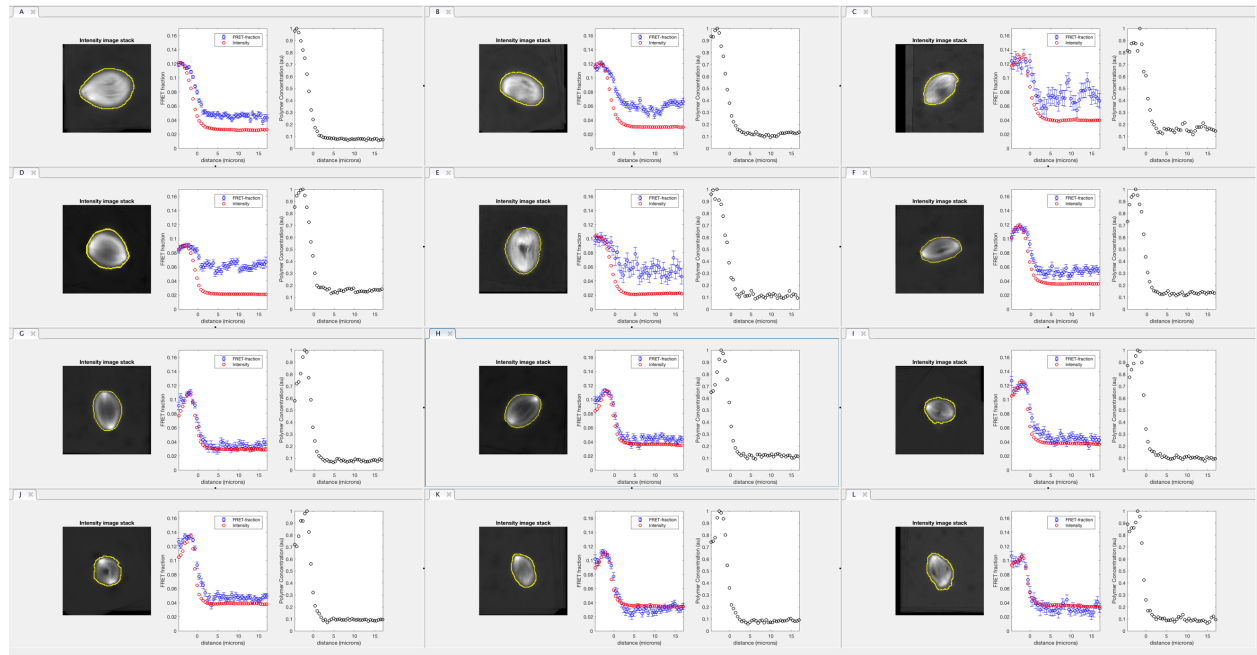


Figure 4.5: Polymer measurements of spindles are similar. The spindle boundary is overlaid in yellow over the spindle. No obvious $\sim 10\mu\text{m}$ gradient can be seen in any of the measurements.

To reduce the noise, we next sought to average these spindles. Weighting the FRET measurement at each distance by the inverse of the standard deviation, we averaged over all 12 spindles at each distance. (Figure 4.6 left). These average FRET and intensity measurements were then used to calculate the average polymer concentration (Figure 4.6 right). No obvious gradient in polymer concentration could be seen. Furthermore, the plateau in polymer concentration is strikingly flat, arguing against the *all nucleation* model. While there may be a $\sim 2 \mu\text{m}$ gradient in polymer concentration, this is very likely due to the density of spindle microtubules having some finite distance over which density falls to zero.

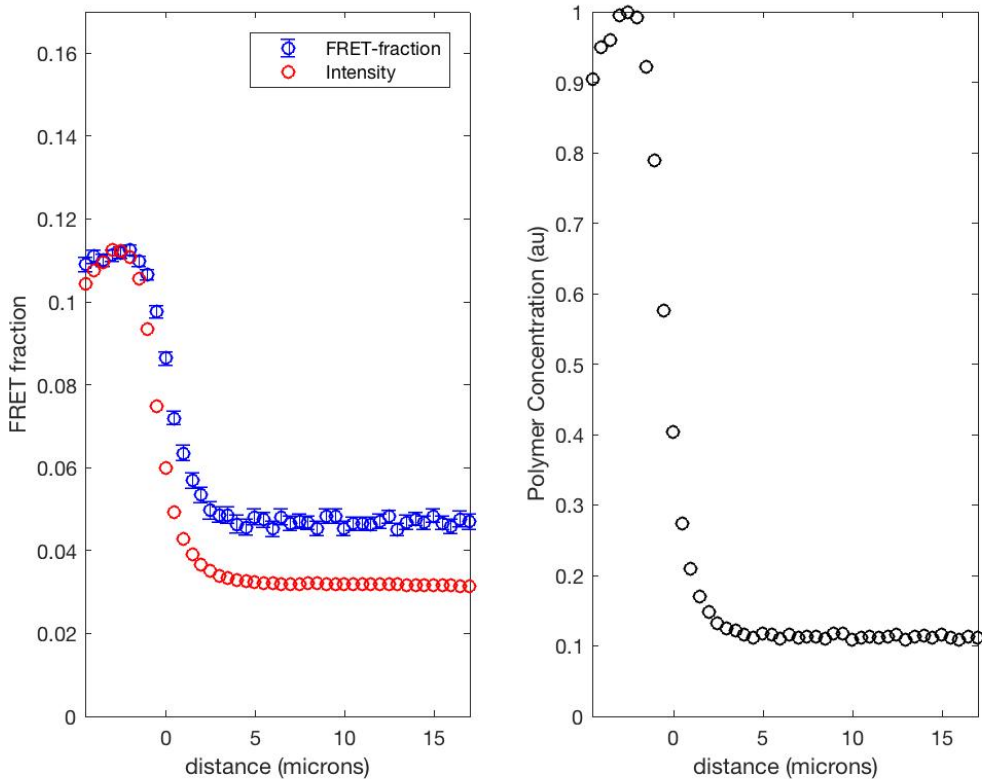


Figure 4.6: The mean FRET fraction, intensity, and polymer concentration of 12 spindles show no obvious gradient in diffusible polymer. (Left) FRET fraction (blue) and intensity (red). Error bars are standard deviation of the posterior distribution of FRET fraction. (Right) Normalized polymer concentration reveals no $\sim 10 \mu\text{m}$ gradient.

The previous measurements were optimized to measure gradients on the 10 μm length scale. However, if there were a gradient on the length scale of 100 μm , it may not be resolvable with measurements that only extend to 20 μm . To test whether a \sim 100 μm gradient existed, we imaged 4 spindles at a low magnification and analyzed the data as previously described. The FRET, intensity, and polymer concentration all exhibit no large length scale gradient. (Figure 4.7).

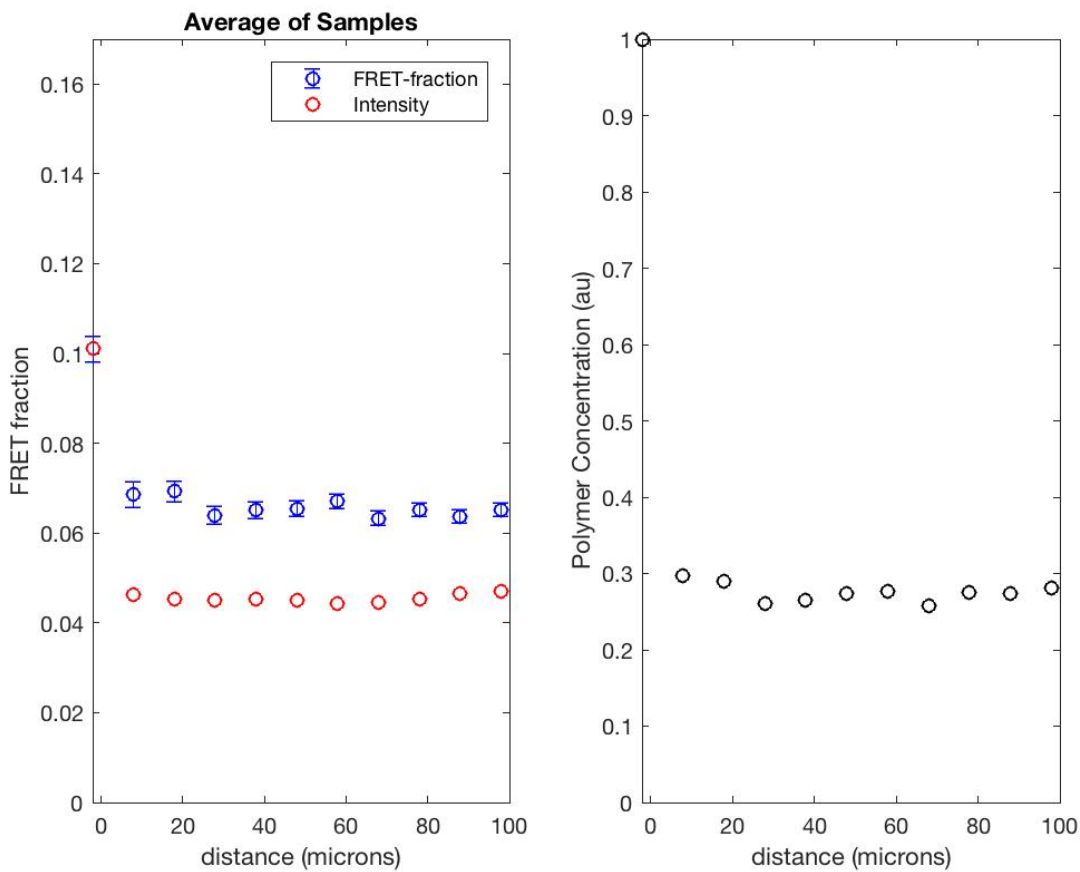


Figure 4.7: Low magnification imaging reveals the lack of a 100 μm length scale gradient in polymer concentration. (A) FRET fraction and intensity measurements. (B) Using the FRET fraction and intensity data in (A), polymer concentration is calculated at each location to obtain a polymer versus distance curve. No long length scale (20-200 μm) gradient in polymer concentration is observed.

Back-of-the-envelope calculations of the *all nucleation* model predict a length scale that is $\sim 10 \mu\text{m}$ or larger. The data argues against this model. Now we turn to more formal modelling to further test the *all nucleation* model and the *bound nucleation* model.

MODEL

In our model, MT's will be generated from nucleation with an initial size ε , grow with a velocity v_g until they switch to a depolymerizing state, at a rate r , at which point they start to depolymerize with velocity v_d until they disappear (i.e., shrink back to their initial size ε). Irrespective of their growth state, MT's will diffuse with an effective diffusivity $\frac{D}{l}$ where l is their current length. In this model the densities $\psi_g(x, l)$ and $\psi_d(x, l)$, which track the number of MT's at position x , whose current length is l , in a growing or depolymerizing state, respectively, will obey the following equations:

$$\partial_t \psi_g(x, l) = -v_g \partial_l \psi_g + \frac{D}{l} \partial_x^2 \psi_g - r \psi_g \quad (\text{Eq 4.1})$$

$$\partial_t \psi_d(x, l) = v_d \partial_l \psi_g + \frac{D}{l} \partial_x^2 \psi_g + r \psi_g \quad (\text{Eq 4.2})$$

This implies the local mass density is:

$$\rho = \int_{\varepsilon}^{\infty} (\psi_g + \psi_d) l dl \quad (\text{Eq 4.3})$$

New microtubules are generated by nucleation at a rate $N(x)$ which is solved for using the boundary condition,

$$\varepsilon v_g \psi_g(x, l = \varepsilon) = N(x) \quad (Eq\ 4.4)$$

The amount $N(x)$ of locally nucleated microtubules is assumed to obey

$$N(x) = \tau_0 + c \frac{\tau_u + \alpha\rho\tau_b}{1 + \alpha\rho} \quad (Eq\ 4.5)$$

where c is the amount of nucleators at location x , τ_0 is the rate of spontaneous nucleation, τ_b is the rate of nucleation generated by bound nucleators and τ_u is the rate of nucleation generated by unbound nucleators. Finally, α is the binding affinity of nucleators for microtubules. Nucleators themselves diffuse in a fashion that is modulated by the presence of microtubules, and deactivate with a rate r_c ,

$$\partial_t c = D_c \partial_x^2 \frac{c}{1 + \alpha\rho} - r_c c \quad (Eq\ 4.6)$$

BOUNDARY CONDITIONS

To find steady states of the model we laid out, we need to complement it with boundary conditions at the interface of the spindle and at infinity. Far from the spindle, all nucleators are presumed to be inactive. Thus,

$$c_\infty = 0 \quad (Eq\ 4.7)$$

This further implies that microtubules far from the spindle must have originated from spontaneous nucleation. Consequently,

$$\varepsilon v_g \psi_g(x \rightarrow \infty, \varepsilon) = \tau_0 \quad (Eq \ 4.8)$$

and sets,

$$\psi_g^\infty = \frac{\tau_0}{\varepsilon v_g} \exp\left(\frac{-r}{\varepsilon v_g}(l - \varepsilon)\right) \quad (Eq \ 4.9)$$

$$\psi_d^\infty = \frac{v_g}{v_d} \frac{\tau_0}{\varepsilon v_g} \exp\left(\frac{-r}{\varepsilon v_g}(l - \varepsilon)\right) \quad (Eq \ 4.10)$$

Our other boundary condition is inside the spindle itself, where we set $\rho_s = 1$, which normalizes all densities such that

$$\psi_g^s = \frac{r^2 v_d}{\varepsilon v_g (\varepsilon r + v_g)(v_d + v_g)} \exp\left(\frac{-r}{v_g}(l - \varepsilon)\right) \quad (Eq \ 4.11)$$

$$\psi_d^s = \frac{v_g}{v_d} \frac{r^2 v_d}{\varepsilon v_g (\varepsilon r + v_g)(v_d + v_g)} \exp\left(\frac{-r}{v_g}(l - \varepsilon)\right) \quad (Eq \ 4.12)$$

Finally, we determine the concentration of nucleator in the from the Eq 4.4 to find

$$c_s = \frac{(\alpha + 1)(\varepsilon r(r v_d - \tau_0(v_d + v_g)) - \tau_0 v_g(v_d + v_g))}{(v_d + v_g)(\alpha \tau_b + \tau_u)(\varepsilon r + v_g)} \quad Eq. \ 4.13$$

To see how polymer concentration changes away from the spindle, we solve this model using the following parameters:

We estimate ε , the smallest length polymer at which it grows and shrinks with normal microtubule dynamics (and therefore is a microtubule) to be 50 nm. We set v_g and v_d to the previously found values of $0.3 \frac{\mu\text{m}}{\text{s}}$ and to $0.9 \frac{\mu\text{m}}{\text{s}}$, respectively. r and r_c was set to the previously measured value of $\frac{1}{17\text{s}}$ (Needleman et al., 2010). The diffusion times unit length for microtubules, D , was to $0.01 \frac{\mu\text{m}^2}{\text{s}}$ (i.e., $0.2 \frac{\mu\text{m}^2}{\text{s}} * \varepsilon$). α is the binding affinity for nucleators to microtubules. Oh et al. measured this for many proposed nucleators and found the largest to be 2 (2016). A smaller α would only make the difference between the models greater (specifically, the *all nucleation* model would have an even longer-length scale polymer gradient), so we use 2 as a worst-case scenario. Finally, we set $\tau_0 = 0$, $\tau_B = \frac{10}{\text{nucleator*s}}$. τ_u is $\frac{10}{\text{nucleator*s}}$ for the *all nucleation* model and 0 for the *bound nucleation* model.

We normalized polymer concentration in the 12 spindles shown in Figure 4.5 to be between 0 and 1. To do this, we found the limiting polymer concentration of the 10 most distal microns and subtracted this value from the polymer concentration. We then rescaled the curves so the maximum was 1. Using numerical methods to solve the model, we find the *bound nucleation* model fits the data well, whereas the *all nucleation* model is very inconsistent with the data (Figure 4.8). These results rule out the *all nucleation model*. However, this data does not rule out the possibility that there is some low-level amount of activity when nucleators are not bound. Future work will entail putting upper bounds on unbound activity. In addition, monomer concentrations can be measured in a spatially resolvable way using the same FRET and intensity measurements. With a few additional assumptions, the *bound nucleation* model can predict the monomer gradient away from the spindle. If the measured monomer gradient is consistent with the model, it may validate the assumptions.

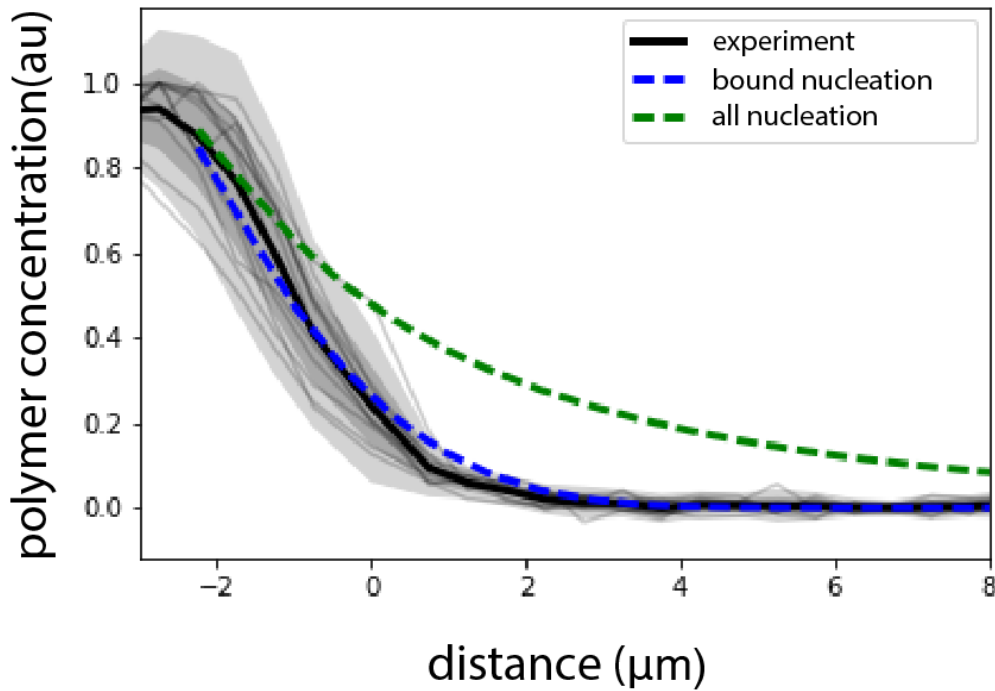


Figure 4.8: The data supports the *bound nucleation* model while strongly arguing against the *all nucleation* model. The *bound nucleation* (blue dashed line) model predicts a sharp ($\sim 2 \mu\text{m}$) gradient in polymer concentration, while the *all nucleation* model (green dashed line) predicts a long ($\sim 10 \mu\text{m}$) gradient in polymer concentration. Polymer concentrations from 12 spindles are shown with grey lines. 1 and 2 standard deviations of these curves are shown in dark grey and light grey, respectively.

M_{ETHODS}

SAMPLE PREPARATION

Samples were measured in a conventional flow cell sealed by candlewax. Bovine tubulin was purified and then labeled with fluorophores as previously described (Mitchison and Kirschner 1984; Hyman et al., 1991, Mitchison lab, 2012). Spindles were assembled in *Xenopus laevis* egg extracts as previously

described (Hannak and Heald, 2006). Tubulin was added to egg extracts by adding donor-labeled tubulin to 1.2 μ M and acceptor-labeled tubulin to 2.0 μ M. Atto565 was used as the donor fluorophore and Atto647N was used as the acceptor fluorophore.

MICROSCOPY

Our microscope system was constructed around an inverted microscope (Eclipse Ti, Nikon, Tokyo, Japan) with a commercial scanning system (DCS-120, Becker & Hickl, Berlin, Germany).

Fluorophores are excited with a Ti:sapphire pulsed laser (Mai-Tai, Spectra-Physics, Mountain View, CA) at a 1000 nm wavelength, 80 MHz repetition rate (\sim 70 fs pulse width), and emitted photons are detected with hybrid detectors (HPM-100-40, Becker & Hickl). The excitation laser was collimated by a telescope assembly to fully utilize the numerical aperture of a water-immersion objective (CFI Apo 40 WI, NA 1.25, Nikon) and avoid power loss at the XY galvanometric mirror scanner. The fluorescence from samples was imaged with a non-descanned detection scheme with a dichroic mirror (705 LP, Semrock) to allow the excitation laser beam to excite the sample while fluorescence passed into the detector path. A short-pass filter was used to further block the excitation laser beam (720 SP, Semrock), followed by an emission filter appropriate for Atto565-labeled tubulin (590/30nm BP, Semrock).

ACQUIRING PHOTON ARRIVAL-TIME HISTOGRAMS

We use a Becker and Hickl Simple-Tau 150 FLIM system to collect photon arrival-time histograms. Arrival times are measured relative to an electric pulse created by a photodiode that is triggered by the excitation laser (Becker, 2010). The TAC range was set to 7×10^{-8} , with a gain of 5, corresponding to a 14 ns maximum arrival time. The TCSPC system can lose fidelity for photons that arrive just before or after the excitation of the photodiode (Becker, 2010), and thus we set the

lower and upper limits to 10.59 and 77.25, respectively, resulting in a \sim 10 ns recording interval. The instrument response was measured using fixed-point illumination of second harmonic generation of a urea crystal. The intensity of the illumination beam was set such that there was an average of \sim 200,000-300,000 photons per second recorded. Data was acquired as a 128x128 pixel image, where a corresponding photon arrival-time histogram was recorded for each pixel.

DATA ANALYSIS

Estimating the FRET fraction and Intensity from Photon Arrival Histograms: We use a Bayesian model to build posterior distributions from photon arrival-time histograms (*Supplemental Materials*). The posterior was evaluated at uniformly spaced grid points in parameter space. Point estimates of the FRET fraction were found by taking the maximum of the posterior distribution of the FRET fraction. To reduce the number of free parameters when analyzing photon arrival histograms to find the FRET fraction, we first found the two lifetimes of the donor fluorophore, and then fixed those lifetimes in our Bayesian analysis. The intensity was corrected for inhomogeneous illumination intensity.

Image Registration: To collect a sufficient number of photons for FLIM analysis of FRET, spindles were required to be imaged for \sim 100 seconds. An acquisition for this duration produces blurry images. Thus, we acquired multiple 10-second acquisitions of spindles and aligned the acquisitions as previously described (Brugués et al., 2010). In short, intensity images are thresholded to include the spindle region. The resulting images are then translated so that the center of mass is centered. Each image is then rotated such that the normalized autocorrelation with the previous frame is maximized. After rotation, the images are translated once more such that the normalized autocorrelation is maximized. Translation and rotation were done using the MATLAB (R2017a) function imtranslate

(with linear interpolation) and imrotation (with no interpolation), respectively.

Image Segmentation: Registered images were segmented by thresholding the spindle to find the boundary of the spindle. Pixels are then segmented into groups by the shortest distance between the pixel and the spindle boundary. Pixels inside the boundary are considered to have a negative distance and pixels outside the spindle are considered to have a positive distance. The photon arrival-time histograms corresponding to each pixel in a group were added together to create the photon arrival-time histogram corresponding to that distance from the spindle boundary. The intensity of this group is calculated as the mean intensity of the pixels in the group.

A

SUPPLEMENTAL MATERIALS

This appendix chapter details and largely reproduces work previously published as Kaye B, Foster PJ, Yoo TY, Needleman DJ (2017). Developing and testing a Bayesian analysis of fluorescence lifetime measurements. PLOS ONE 12, e0169337.

In chapter 3 we performed Bayesian analysis on photon arrival histograms by first constructing a probabilistic model for the lifetime of donors engaged in FRET, the lifetime of donors not engaged in FRET, the fraction of photons from donors engaged in FRET, the fraction of donors not engaged in FRET, and the fraction of photons from background (i.e. stray light and detector dark noise); which is directly based on previous work (Kaye, Foster, Yoo et al., 2017; Rowley et al., 2011, Rowley et al., 2016). Photon arrival-times are discretized into time bins. It has been shown that the likelihood of observing a particular photon arrival histogram is:

$$\begin{aligned} & \text{Prob}(\{\text{data}\} | w_F, \tau_F, w_{NF}, \tau_{NF}, w_B) \\ &= \prod_j [w_F \text{Prob}(P \in b_j | w_F, \tau_F, P \in P_F) \\ & \quad + w_{NF} \text{Prob}(P \in b_j | P \in w_{NF}, \tau_{NF}, P \in P_{NF}) + w_B \text{Prob}(P \in b_j | w_B, P \in P_B)]^{P_j} \end{aligned}$$

where the number of photons that arrived in the j^{th} bin is P_j ; w_F and w_{NF} are the fraction of photons emitted from donors engaged and not engaged in FRET, respectively, and the fraction from background is w_B ; τ_F and τ_{NF} are the lifetimes from donors engaged and not engaged in FRET, respectively; $P \in P_F$, $P \in P_{NF}$, and $P \in P_B$ signify that the photon originated from donors engaged in FRET, not engaged in FRET, or background, respectively; $P \in b_j$ signifies a photon arriving in the j^{th} bin (Kaye, Foster, Yoo et al., 2017). This likelihood can be derived assuming that photon arrival

times are independent of each other. We use a uniform prior and thus the posterior distribution is equal to the likelihood.

The likelihood is modified to account for time bins for which the measurement system is unable to record photons or for time bins that are removed post-measurement to filter out spurious signals.

The modified likelihood is:

$$\begin{aligned} & \text{Prob}(\{\text{data}\} | w_F, \tau_F, w_{NF}, \tau_{NF}, w_B) \\ &= \prod_j \left[\frac{a}{D} w_F \text{Prob}(P \in b_j | w_F, \tau_F, P \in P_F) \right. \\ & \quad \left. + \frac{b}{D} w_{NF} \text{Prob}(P \in b_j | P \in w_{NF}, \tau_{NF}, P \in P_{NF}) + \frac{c}{D} w_B \text{Prob}(P \in b_j | w_B, P \in P_B) \right]^{P_j} \end{aligned}$$

where

$$a = \frac{\sum^{\text{kept time bins}} \text{prob}(P \in b_j | P \in w_F, \tau_F)}{\sum^{\text{all time bins}} \text{prob}(P \in b_j | P \in w_F, \tau_F)}$$

$$b = \frac{\sum^{\text{kept time bins}} \text{prob}(P \in b_j | P \in w_{NF}, \tau_{NF})}{\sum^{\text{all time bins}} \text{prob}(P \in b_j | P \in w_{NF}, \tau_{NF})}$$

$$c = \frac{\sum^{\text{kept time bins}} \text{prob}(P \in b_j | P \in w_B, \tau_\infty)}{\sum^{\text{all time bins}} \text{prob}(P \in b_j | P \in w_B, \tau_\infty)}$$

$$D = w_F a + w_{NF} b + w_B c$$

The system measures the photon arrival time by measuring the time between a reference pulse and the time a photon is recorded (Becker, 2010). The *instrument response function* is the response of the system to a delta-function excitation, measured here by second harmonic generation of a urea crystal. The probability density function for photon arrival times, $\text{prob}(P \in b_j | P \in w, \tau)$, relative to excitation, is found by convolving the photon emission from the fluorophore, as described by Eq. 3.1, with the instrument response function,

$$\text{prob}(P \in b_j | P \in w, \tau) \propto \int_0^{\infty} e^{-x/\tau} \text{IRF}(x - t) dx$$

where IRF is the instrument response function. Photon fractions (w_F, w_{NF}, w_B) are related to the fraction of donors engaged in FRET (F in Eq. 3.1) by:

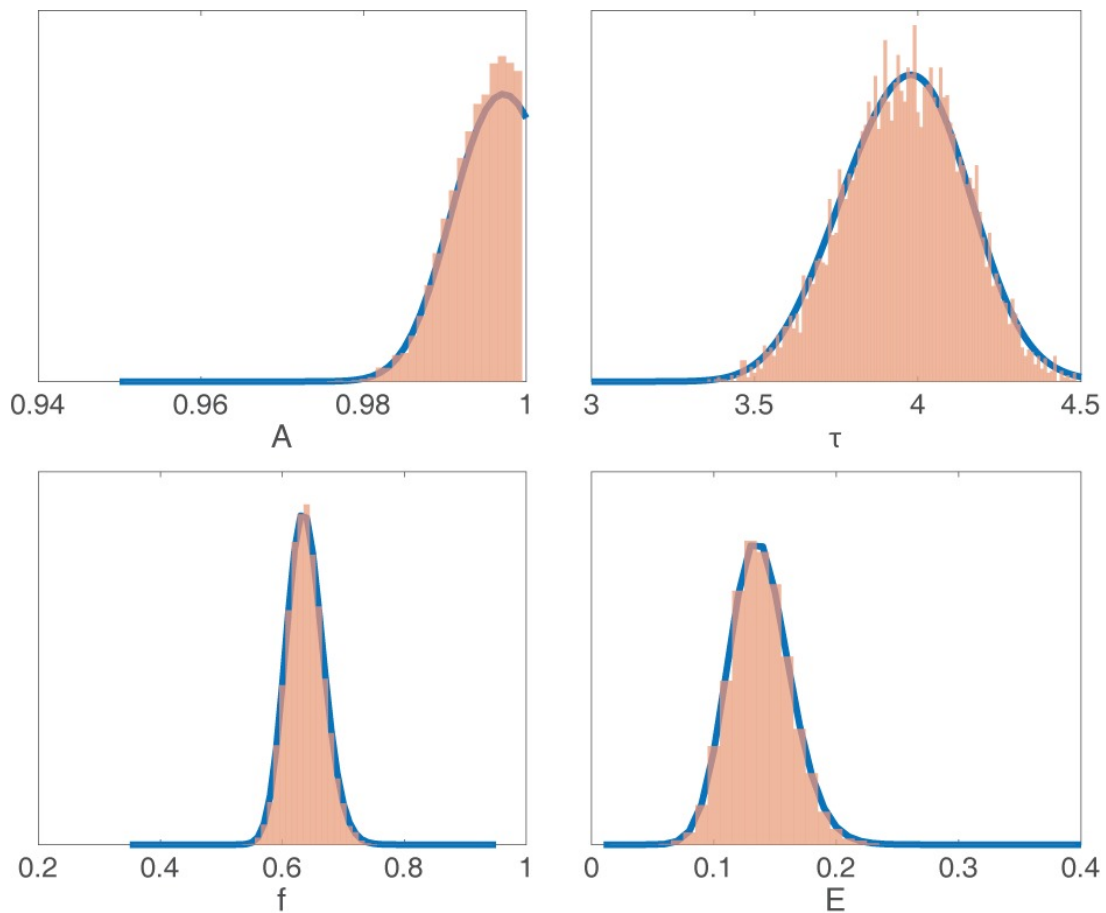
$$F = \frac{w_F}{w_F + \alpha w_{NF}}$$

The system has increased sensitivity to recording photons for certain time bins. This means the probability of a photon being recorded in the j^{th} bin, given a photon arrived within that bin, depends on the bin number. We account for this effect by dividing out the number of photons in each bin, P_j , by the relative sensitivity in each bin. The relative sensitivity is found by recording uncorrelated stray light.

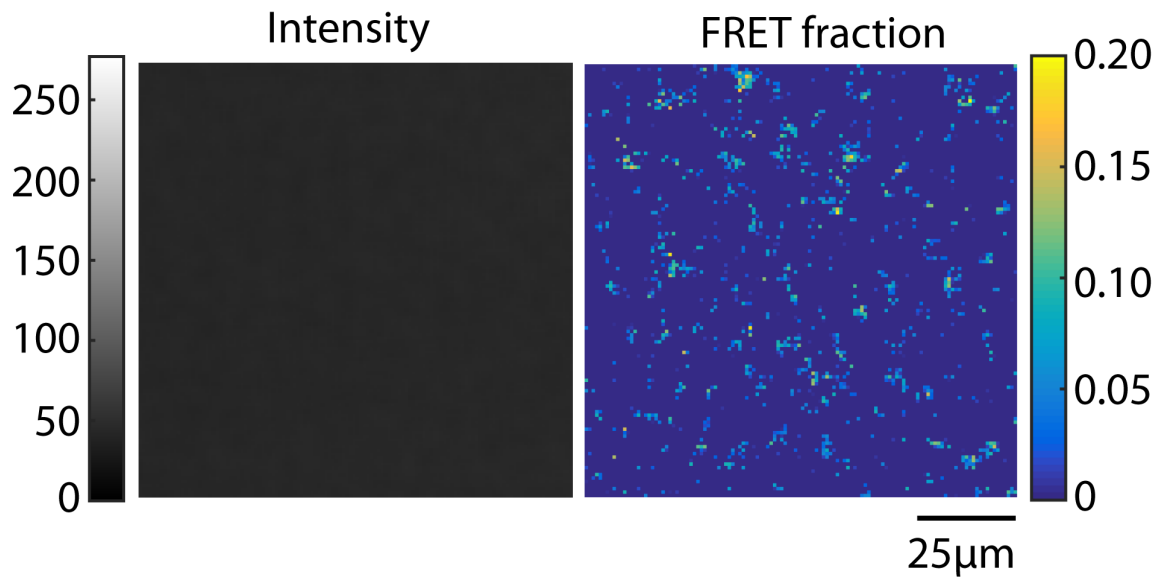
B

SUPPLEMENTAL FIGURES

This appendix chapter details and largely reproduces work previously published as Kaye B, Foster PJ, Yoo TY, Needleman DJ (2017). Developing and testing a Bayesian analysis of fluorescence lifetime measurements. PLOS ONE 12, e0169337 and Kaye B, Yoo TY, Foster PJ, Yu C, Needleman DJ (2017). Bridging length scales to measure polymer assembly. Molecular Biology of the Cell.



Supplemental Figure S2.1. Posterior distributions generated using grid points and stochastic optimization are equivalent. Results from Markov chain Monte Carlo (red) and grid points (blue) were generated from the same data set.



Supplemental Figure S3.1: An intensity image (left) and corresponding FRET fraction map (right) when donor and acceptor labeled tubulin is added to *Xenopus* egg extract without inducing microtubule formation.

REFERENCES

- Allen C and Borisy G (1974). Structural polarity and directional growth of microtubules of *Chlamydomonas Flagella*. Journal of Molecular Biology 90, 381-402.
- Bastiaens PI, Squire, A (1999). Fluorescence lifetime imaging microscopy: spatial resolution of biochemical processes in the cell. Trends in Cell Biology 9, 48–52.
- Becker, W (2010). The bh TCSPC Handbook, Berlin: Becker and Hickl GmbH.
- Belomont L and Mitchison TJ (1996). Identification of a Protein That Interacts with Tubulin Dimers and Increases the Catastrophe Rate of Microtubules. Cell 84, 623-631.
- Bird DK, Yan L, Vrotsos KM, Eliceiri KW, Vaughan EM, Keely PJ, et al. (2005) Metabolic mapping of MCF10A human breast cells via multiphoton fluorescence lifetime imaging of the coenzyme NADH. Cancer Research 65, 8766–8773. doi: 10.1158/0008-5472.CAN-04-3922 PMID: 16204046
- Boens N, Qin W, Basarić N, Hofkens J, Ameloot M, Pouget J, et al (2007). Fluorescence Lifetime Standards for Time and Frequency Domain Fluorescence Spectroscopy. Analytical Chemistry 79, 2137–2149. doi: 10.1021/ac062160k PMID: 17269654
- Bordas J, Mandelkow EM, Mandelkow E (1983). Stages of tubulin assembly and disassembly studied by time-resolved synchrotron X-ray scattering. Journal of Molecular Biology 164, 89–135.
- Brinkley BR (1985). Microtubule organizing centers. Annual Review of Cell Biology 1, 145-172.
- Brugués J, Needleman DJ (2010). Nonequilibrium fluctuations in metaphase spindles: Polarized light microscopy, image registration, and correlation functions. International Society for Optics and Photonics, 76180L–76180L
- Brugués J, Nuzzo V, Mazur E, Needleman DJ (2012). Nucleation and transport organize microtubules in metaphase spindles. Cell 149, 554–564.
- Brugués J, Needleman DJ (2014). Physical basis of spindle self-organization. Proceedings of the National Academy of Sciences 111, 18496–18500.
- Chen W, Avezov E, Schlachter SC, Gielen F, Laine RF, Harding HP, et al (2015). A method to quantify FRET stoichiometry with phasor plot analysis and acceptor lifetime ingrowth. Biophysical Journal 108, 1002. doi: 10.1016/j.bpj.2015.01.012 PMID: 25762312
- Colyer RA, Siegmund OHW, Tremsin AS, Vallerga JV, Weiss S, Michalet X (2012). Phasor imaging with a widefield photon-counting detector. Journal of Biomedical Optics 17, 016008. doi: 10.1117/1.JBO.17.1.016008 PMID: 22352658

- Cooper JA, Buhle EL, Walker SB, Tsong TY, Pollard TD (1983). Kinetic evidence for a monomer activation step in actin polymerization. *Biochemistry* 22, 2193–2202.
- Cox MM (2001). Historical overview: searching for replication help in all of the rec places. *Proceedings of the National Academy of Sciences* 98, 8173–8180.
- Cantor CR, Schimmel PR (1980). Biophysical Chemistry Part 2: Techniques for the study of biological structure and function, New York: W.H. Freeman and Company.
- Chang C, Sud D, Mycek MA (2007). Fluorescence Lifetime Imaging Microscopy. *Methods of Cell Biology* 81, 495–524. doi: 10.1016/S0091-679X(06)81024-1 PMID: 17519182
- Curmi P, Andersen S, Lachkar S, Gavet O, Karsenti E, Knossow M, Sobel A (1997). The Stathmin/Tubulin Interaction *in Vitro*. *The Journal of Biological Chemistry* 272, 25029-25036.
- Desai A, Mitchison TJ (1997). Microtubule polymerization dynamics. *Cell and Developmental Biology* 13, 83–117.
- Dokland T (2000). Freedom and restraint: themes in virus capsid assembly. *Structure* 8, 157–162.
- Dumont J, Desai A (2012). Acentrosomal spindle assembly and chromosome segregation during oocyte meiosis. *Trends in Cell Biology* 5, 241-249.
- Fletcher DA, Mullins RD (2010). Cell mechanics and the cytoskeleton. *Nature* 463, 485–492.
- Flyvbjerg H, Jobs E (1996). Kinetics of self-assembling microtubules: an “inverse problem” in biochemistry. *Proceedings of the National Academy of Sciences* 93, 5975–5979.
- Flyvbjerg H and Jobs E (1997). Microtubule dynamics II. Kinetics of self-assembly. *Physical Review E*, 56-6, 7083-7099.
- Foster PJ, Fürthauer S, Shelley MJ, Needleman DJ (2015). Active contraction of microtubule networks. *eLife* 4, e10837.
- Frieden C (1983). Polymerization of Actin: Mechanism of the Mg²⁺-Induced Process at pH 8 and 20°C. *Proceedings of the National Academy of Sciences* 80, 6513–6517.
- Frieden C and Goddette DW (1983). Polymerization of actin and actin-like systems: evaluation of the time course of polymerization in relation to the mechanism. *Biochemistry* 22, 5836–5843.
- Frieden C (1985). Actin and tubulin polymerization: the use of kinetic methods to determine mechanism. *Annual Review of Biophysics and Biophysical Chemistry*, 14, 189–210.
- Fygenson DK, Flyvbjerg H, Sneppen K, Libchaber A, Leibler S (1995). Spontaneous nucleation of microtubules. *Physical Review E* 51(5), 5058–5063.

- Gaetz J, Kapoor TM (2004). Dynein/dynactin regulate metaphase spindle length by targeting depolymerizing activities to spindle poles. *The Journal of cell biology*, 166, 465–471.
- Garner EC, Campbell CS, Mullins RD (2004). Dynamic instability in a DNA-segregating prokaryotic actin homolog. *Science*, 306, 1021-1025.
- Gatlin JC, Matov A, Groen A, Needleman DJ, Maresca TJ, Danuser G, Mitchison TJ, and Salmon ED (2009). Spindle fusion requires dynein mediated sliding of oppositely oriented microtubules. *Current Biology* 19, 287–296.
- Gerritsen HC, Sanders R, Draaijer A, Ince C (1997). Fluorescence lifetime imaging of oxygen in living cells. *Journal of Fluorescence* 7, 11–15. doi: 10.1007/BF02764572
- Gigant B, Curmi P, Martin-Barbey C, Charbaut E, Lachkar S, Lebeau L, Slavoshian S, Sobel A, Knossow M (2000). The 4 Å X-Ray Structure of a Tubulin: Stathmin-like Domain Complex. *Cell*, 102, 809-816.
- Grimm JB, English BP, Chen J, Slaughter JP, Zhang Z, Revyakin, A, Patel R, Macklin JJ, Normanno D, Singer RH, Lionnet T, Lavis LD (2015). A general method to improve fluorophores for live-cell and single-molecule microscopy. *Nature Methods* 12(3), 244–250.
- Hannak E, Heald R (2006). Investigating mitotic spindle assembly and function in vitro using *Xenopus laevis* egg extracts. *Nature Protocols* 1, 2305–2314.
- Heald R, Tournebize R, Blank R, Sandaltzopoulos R, Becker P, Hyman A, Karsenti E (1996). Self-organization of microtubules into bipolar spindles around artificial chromosomes in *Xenopus* egg extracts. *Nature* 382, 420–425.
- Helmke KJ, Heald R (2014). TPX2 levels modulate meiotic spindle size and architecture in *Xenopus* egg extracts. *The Journal of Cell Biology* 206, 385-393.
- Hiller G, & Weber K (1978). Radioimmunoassay for tubulin: a quantitative comparison of the tubulin content of different established tissue culture cells and tissues. *Cell* 14, 795-804.
- Hinde E, Digman MA, Hahn KM (2013). Millisecond spatiotemporal dynamics of FRET biosensors by the pair correlation function and the phasor approach to FLIM. *Proceedings of the National Academy of Sciences* 110(1), 135–140.
- Ho C. M., Hotta T, Kong Z, Zeng CJ, Sun J, Lee YR, Liu B (2011). Augmin plays a critical role in organizing the spindle and phragmoplast microtubule arrays in *Arabidopsis*. *Plant Cell* 23, 2606–2618.
- Hsia K. C, Wilson-Kubalek EM, Dottore A, Hao Q, Tsai KL, Froth S, Shimamoto Y, Milligan RA, TM Kapoor. Reconstitution of the augmin complex provides insights into its architecture and function. *Nature Cell Biology* 16, 852–863 (2014).
- Hyman A, Drechsel D, Kellogg D, Salser S, Sawin K, Steffen P, Wordeman L, Mitchison TJ (1991). Preparation of modified tubulins. *Methods Enzymology* 196, 478-485.

- Inoue S. and Sato H. (1967). Cell motility by labile association of molecules. The nature of mitotic spindle fibers and their role in chromosome movement. *Journal of General Physiology* 50, 259–292.
- Kamasaki T, O'Toole E, Kita S, Osumi M, Usukura J, McIntosh R, Goshima G. (2013) Augmin-dependent microtubule nucleation at microtubule walls in the spindle. *Journal of Cell Biology* 202, 25–33.
- Katen S, Zlotnick A (2009). The thermodynamics of virus capsid assembly. *Methods in Enzymology* 455, 395–417.
- Kaye B, Foster PJ, Yoo TY, Needleman DJ (2017). Developing and Testing a Bayesian Analysis of Fluorescence Lifetime Measurements. *PLoS ONE* 12(1): e0169337.
- Keating TJ, Borisy GG (2000). Immunostructural evidence for the template mechanism of microtubule nucleation. *Nature Cell Biology* 6, 352-357.
- Khodjakov A, Cole RW, Oakley BR, Rider CL (2000). Centrosome-independent mitotic spindle formation in vertebrates. *Current Biology* 10, 59-67.
- Köllner M, Wolfrum J (1992). How many photons are necessary for fluorescence-lifetime measurements? *Chemical Physics Letters*. 200: 199–204. doi: 10.1016/0009-2614(92)87068-Z
- Kollman JM, Polka JK, Zelter A, Davis TN, Agard DA (2010) Microtubule nucleating gamma-TuSC assembly with 13-fold microtubule-like symmetry. *Nature*, 466 879-882.
- Kollman JM, Merdes A, Mourey L, Agard DA (2011). Microtubule nucleation by γ -tubulin complexes. *Nat. Rev. Mol. Cell Biol.* 12, 709–721.
- Lakowicz JR (2006). *Principles of fluorescence spectroscopy*, Maryland: Springer.
- Lin H-J, Herman P, Lakowicz JR (2003). Fluorescence lifetime-resolved pH imaging of living cells. *Cytometry* 52A, 77–89. doi: 10.1002/cyto.a.10028 PMID: 12655651
- Lüders, J., Patel, U. K. & Stearns, T (2005). GCP-WD is a γ -tubulin targeting factor required for centrosomal and chromatin-mediated microtubule nucleation. *Nature Cell Biology* 8, 137–147.
- Mahoney, NM, Goshima, G, Douglass, AD, Vale RD (2006). Making microtubules and mitotic spindles in cells without functional centrosomes. *Current Biology* 16, 564–569.
- Matsudaira P, Bordas J, Koch MH (1987). Synchrotron x-ray diffraction studies of actin structure during polymerization. *Proceedings of the National Academy of Sciences* 84, 3151–3155.
- Megraw TL, Kao LR, Kaufman TC (2001). Zygotic development without functional mitotic centrosomes. *Current Biology* 11, 116-120.
- Merdes A, Heald R, Samejima K, Earnshaw WC, Cleveland DW (2000). Formation of spindle poles by dynein/dynactin-dependent transport of NuMA. *The Journal of cell biology* 149, 851–861.

- Mertz J (2010). Introduction to Optical Microscopy, Colorado: Roberts and Company Publishers.
- Meyer RR, Laine PS. (1990). The single-stranded DNA-binding protein of Escherichia coli. *Microbiological Reviews* 54, 342-380.
- Mitchison Lab (2012). Labeling Tubulin and Quantifying Labeling Stoichiometry. Available at <http://mitchison.med.harvard.edu/protocols.html>. Accessed May 22, 2015.
- Mitchison T & Kirschner M (1984). Microtubule assembly nucleated by isolated centrosomes. *Nature* 312, 232–237.
- Moritz M, Braunfeld MB, Guénebaut V, Heuser J, Agard DA (2000). Structure of the gamma-tubulin complex: a template for microtubule nucleation. *Nature Cell Biology* 6, 365-370.
- Mullins DR, Heuser JA, Pollard TD (1998). The Interaction of Arp2/3 Complex with Actin: Nucleation, High Affinity Pointed End Capping, and Formation of Branching Networks of Filaments. *Proceedings of the National Academy of Sciences* 95, 6181-6186.
- O'Connell JD, Zhao A, Ellington AD, Marcotte EM (2012). Dynamic reorganization of metabolic enzymes into intracellular bodies. *Cell and Developmental Biology* 28, 89–111.
- Oh D, Yu C-H, Needleman D (2016). Spatial organization of the Ran pathway by microtubules in mitosis. *Proceedings of the National Academy of Sciences*, 113-31, 8729-8734.
- Ohba T, Nakamura M, Nishitani H, Nishimoto T (1999). Self-organization of microtubule asters induced in Xenopus egg extracts by GTP-bound Ran. *Science*, 284, 1356–1358.
- Okamoto K & Hayashi Y (2006). Visualization of F-actin and G-actin equilibrium using fluorescence resonance energy transfer (FRET) in cultured cells and neurons in slices. *Nature Protocols* 1, 911–919.
- Oosawa F, & Kasai M (1962). A theory of linear and helical aggregations of macromolecules. *Journal of Molecular Biology*.
- Parsons SF & Salmon ED (1997). Microtubule assembly in clarified Xenopus egg extracts. *Cell Motility and the Cytoskeleton* 36:1–11.
- Peter M, Ameer-Beg SM, Hughes MKY, Keppler MD, Prag S, Marsh M, et al (2005). Multiphoton-FLIM quantification of the EGFP-mRFP1 FRET pair for localization of membrane receptor-kinase interactions. *Biophysical Journal* 88, 1224–1237. doi: 10.1529/biophysj.104.050153 PMID: 15531633
- Petrovska I, Nüske E, Munder MC, Kulasegaran G, Malinovska L, Kroschwald S, Richter D, Fahmy K, Gibson K, Verbavatz JM, Alberti S (2014). Filament formation by metabolic enzymes is a specific adaptation to an advanced state of cellular starvation. *eLife* 3, e02409.
- Petry, S., Pugieux, C., Nedelec, F.J., and Vale, R.D. (2011). Augmin promotes meiotic spindle formation and bipolarity in *Xenopus* egg extracts. *Proc. Natl. Acad. Sci. USA* 108, 14473–14478.

- Petry S, Groen AC, Isihara K, Mitchison TJ, Vale RD (2013). Branching microtubule nucleation in Xenopus egg extract mediated by augmin and TPX2. *Cell* 152, 768–777.
- Pollard TD, Cooper JA (1986). Actin and actin-binding proteins. A critical evaluation of mechanisms and functions. *Annual Review of Biochemistry* 55, 987–1035.
- Pollard TD (1990). Actin. *Current Opinion in Cell Biology* 2, 33–40.
- Rohatgi R, Nollau P, Ho HY, Kirschner MW, Mayer BJ (2001). Nck and phosphatidylinositol 4,5-bisphosphate synergistically activate actin polymerization through the N-WASP-Arp2/3 pathway. *The Journal of Biological Chemistry* 276, 26448–26452.
- Roll-Mecak A, Vale RD (2006). Making more microtubules by severing: a common theme of noncentrosomal micro-tubule arrays? *Journal of Cell Biology* 175, 849–851.
- Rowley MI, Barber PR, Coolen AC, Vojnovic B (2011). Bayesian analysis of fluorescence lifetime imaging data. Presented at the Proceedings of the SPIE 7903, 790325–790321.
- Rowley MI, Coolen ACC, Vojnovic B, Barber PR (2016). Robust Bayesian Fluorescence Lifetime Estimation, Decay Model Selection and Instrument Response Determination for Low-Intensity FLIM Imaging. *PLoS ONE* 11(6): e0158404.
- Roy R, Hohng S, Ha T (2008). A practical guide to single-molecule FRET. *Nature Methods*. 5: 507–516. doi: 10.1038/nmeth.1208 PMID: 18511918
- Salmon ED, Leslie RJ, Saxton WM, Karow ML, and McIntosh JR (1984). Spindle microtubule dynamics in sea urchin embryos: analysis using a fluorescein-labeled tubulin and measurements of fluorescence redistribution after laser photobleaching. *Journal of Cell Biology* 99, 2165–2174.
- Sept D, McCammon JA (2001). Thermodynamics and Kinetics of Actin Filament Nucleation. *Biophysical Journal* 81, 667–674.
- Sawin KE, LeGuellec K, Philippe M, and Mitchison T (1992). “Mitotic spindle organization by a plus-end-directed microtubule motor.” *Nature* 359, 540–543.
- Sharman KK, Periasamy A, Ashworth H, Demas JN (1999). Error analysis of the rapid lifetime determination method for double-exponential decays and new windowing schemes. *Analytical Chemistry* 71, 947–952. doi: 10.1021/ac981050d PMID: 21662765
- Sivia D, Skilling J (2006). Data Analysis: A Bayesian Tutorial. 2nd ed. New York: Oxford University Press.
- Stachowiak JC, Schmid EM, Ryan CJ, Ann HS, Sasaki DY, Sherman MB, et al (2012). Membrane bending by protein–protein crowding. *Nature Cell Biology* 14, 944–949. doi: 10.1038/ncb2561 PMID: 22902598.

- Stringari C, Cinquin A, Cinquin O (2011). Phasor approach to fluorescence lifetime microscopy distinguishes different metabolic states of germ cells in a live tissue. pp. 13582–13587.
- Taylor DL, Reidler J, Spudich JA, Stryer L (1981). Detection of actin assembly by fluorescence energy transfer. *Journal of Cell Biology* 89, 362–367.
- Tellam R, Frieden C (1982). Cytochalasin D and platelet gelsolin accelerate actin polymer formation. A model for regulation of the extent of actin polymer formation in vivo. *Biochemistry* 21, 3207–3214.
- Tobacman, LS, Korn ED (1983). The Kinetics of Actin Nucleation and Polymerization. *Journal of Biological Chemistry* 258, 3207-3214.
- Verde F, Berrez JM, Antony C, Karsenti E (1991). Taxol-induced microtubule asters in mitotic extracts of Xenopus eggs: requirement for phosphorylated factors and cytoplasmic dynein. *The Journal of Cell Biology* 112: 1177–1187.
- Voter WA, Erickson HP (1984). The kinetics of microtubule assembly. Evidence for a two-stage nucleation mechanism. *The Journal of Biological Chemistry*, 259, 10430–10438.
- Wallrabe H, Periasamy A (2005). Imaging protein molecules using FRET and FLIM microscopy. *Current Opinion in Biotechnology*. 16: 19–27. doi: 10.1016/j.copbio.2004.12.002 PMID: 15722011
- Wang YL, Taylor DL (1981). Probing the dynamic equilibrium of actin polymerization by fluorescence energy transfer. *Cell* 27, 429–436.
- Wieczorek M, Bechstedt S, Chaaban S, Brouhard GJ (2015). Microtubule-associated proteins control the kinetics of microtubule nucleation. *Nature Cell Biology* 17, 907–916.
- Wegner A, Engel J (1975). Kinetics of the cooperative association of actin to actin filament. *Biophysical Chemistry* 3, 215–225.
- Wen KK, Rubenstein PA (2009). Differential Regulation of Actin Polymerization and Structure by Yeast Formin Isoforms. *Journal of Biological Chemistry* 284, 16776–16783.
- Widlund Per, Podolski M, Reber S, Alper J, Storch M, Hyman A, Howard J, Drechsel D. (2012). One-step purification of assembly-competent tubulin from diverse eukaryotic sources. *Molecular Biology of the Cell* 23, 4394-4401.
- Wieczorek M, Bechstedt S, Chaaban, S & Brouhard GJ (2015). Microtubule-associated proteins control the kinetics of microtubule nucleation. *Nature Cell Biology* 17, 907–916.
- Wiese C, Wilde A, Moore MS, Adam SA, Merdes A, Zheng Y (2001). Role of importin-beta in coupling Ran to downstream targets in microtubule assembly. *Science* 291, 653–656.
- Yoo TY, Needleman DJ (2016). Studying Kinetochores In Vivo Using FLIM-FRET. The Mitotic Spindle. New York, NY: Springer New York pp. 169–186. doi: 10.1007/978-1-4939-3542-0_11

Zhang H, Dawe RK (2011). Mechanisms of plant spindle formation. Chromosome Research 3, 335-344.

Zlotnick A, Johnson JM, Wingfield PW, Stahl SJ, Endres D (1999). A theoretical model successfully identifies features of hepatitis B virus capsid assembly. Biochemistry 38, 14644–14652.